



Interaction between small-scale mantle diapirs and a continental root

P. van Thienen and A. P. van den Berg

*Department of Theoretical Geophysics, University of Utrecht, P. O. Box 80.021, 3508 TA Utrecht, Netherlands
(thienen@geo.uu.nl; berg@geo.uu.nl)*

J. H. de Smet

Department of Theoretical Geophysics, University of Utrecht, P. O. Box 80.021, 3508 TA Utrecht, Netherlands

*Now at Portfolio Modelling, ING Credit Risk Management, P. O. Box 1800, 1000 BV Amsterdam, Netherlands.
(jeroen.de.smet@ingbank.com)*

J. van Hunen

Department of Theoretical Geophysics, University of Utrecht, P. O. Box 80.021, 3508 TA Utrecht, Netherlands

*Now at Department of Physics, University of Colorado, 390 UCB, Boulder, CO 80309-0390, USA.
(jeroen.vanhunen@colorado.edu)*

M. R. Drury

*Department of Structural Geology, University of Utrecht, P. O. Box 80.021, 3508 TA Utrecht, Netherlands
(martynd@geo.uu.nl)*

[1] A possible mechanism for adding material to a continental root is by means of upwellings from the convecting mantle subject to pressure release partial melting. We present results of numerical modeling of the interaction of melting diapirs with continental roots in an Archean setting characterized by a mantle potential temperature of 1750°C in a two-dimensional (2-D) Cartesian geometry. In an extension of earlier work [de Smet *et al.*, 2000b] we have investigated the influence of mantle rheology on the behavior of diapirs. We have in particular looked at the difference in behavior of diapirs using a composite rheology combining both grain size sensitive diffusion creep and dislocation creep mechanisms. We have used the grain size, here taken to be uniform, as a control parameter to obtain model cases with varying contribution from the two creep mechanisms. The diapirs in the composite rheology model rise much faster than they do in a purely Newtonian model. Observed diapiric ascent times from 230 km depth to the top of the ascent path at about 80 km depth are approximately 1 Myr for a Newtonian model (averaged 14 cm/yr) compared to about 50 thousand years for a composite rheology model (averaged 3 m/yr) with the same parameters for the Newtonian component. This clearly indicates the large impact of the dislocation creep component of the viscous deformation process. We have also investigated the effect of an increase in the viscosity due to dehydration during partial melting. This increase has a strong influence on the development of rising diapirs. The ascent velocity and lateral spreading of the diapirs at the end of their ascent are effectively reduced when a viscosity increase by a factor of 10 is applied, and the effect becomes stronger for larger factors. Average vertical velocities range from 1.4 cm/yr for a factor 10 to 2 mm/yr for a factor 200. The most striking result of the viscosity increase due to dehydration is the reduction of the ascent velocity, thereby stretching the characteristic timescale of the diapiric intrusion process to a value between 5 and 50 Myr for dehydration viscosity prefactor values of 10 and 200, respectively. In contrast with the strong difference between the Newtonian and the composite rheology models, small differences are found in the

overall dynamics between the composite rheological models, characterized by different values of the uniform grain size. The composite rheological models exhibit self-regulating behavior where substantial differences between the relative contributions of the two creep components result in very similar effective viscosities, due to a local dominance of dislocation creep at high stresses and corresponding similar flow dynamics. Stress levels and P,T paths in the modeling results are consistent with estimates obtained from Precambrian peridotite bodies which are interpreted to have originated from asthenospheric diapirism.

Components: 13,000 words, 17 figures, 5 tables, 2 videos.

Keywords: continental roots; numerical modeling; mantle diapirs; Archean; creep mechanisms; water.

Index Terms: 3210 Mathematical Geophysics: Modeling; 3902 Mineral Physics: Creep and deformation; 8120 Tectonophysics: Dynamics of lithosphere and mantle—general; 8121 Tectonophysics: Dynamics, convection currents and mantle plumes; 8160 Tectonophysics: Evolution of the Earth: Rheology—general.

Received 4 March 2002; **Revised** 26 July 2002; **Accepted** 5 December 2002; **Published** 18 February 2003.

van Thienen, P., A. P. van den Berg, J. H. de Smet, J. van Hunen, and M. R. Drury, Interaction between small-scale mantle diapirs and a continental root, *Geochem. Geophys. Geosyst.* 4(2), 8301, doi:10.1029/2002GC000338, 2003.

Theme: Thermochemical Convection in the Earth's Interior

Guest Editor: Peter van Keken, Louis Moresi, and Adrian Lenardic

1. Introduction

[2] Numerical modeling experiments have shown that mantle diapirs could be important agents in the growth of continental roots during the Archean and Proterozoic [*de Smet et al.*, 1998]. These mantle diapirs are generally on a scale of 50 to 100 km and penetrate an existing root while producing melt, and a complementary depleted low density residue, thus adding depleted material to the continental root. Plumes rising through the mantle are strongly influenced by the type of rheology.

[3] The two important deformation mechanisms in the upper mantle are diffusion creep and dislocation creep [*Karato and Wu*, 1993]. Diffusion creep takes place through diffusion of mass between grain boundaries. The strain rate increases linearly with applied stress, and decreases in a power law fashion with the grain size. Dislocation creep, on the other hand, takes place through the transport of dislocations in the crystal structure. It has a power law relation between applied stress and resulting strain rate (nonlinear), and it is insensitive to grain size [*Karato and Wu*, 1993]. The viscosity corresponding to dislocation creep flow decreases with

increasing stress, a phenomenon known as shear-thinning. For the present mantle, dislocation creep is generally the dominant mechanism in the asthenosphere, whereas diffusion creep dominates in the lithospheric mantle and in the deeper upper mantle and lower mantle [*Karato et al.*, 1995; *van den Berg and Yuen*, 1996]. Since olivine is the weakest major phase in mantle peridotite, the rheology of the upper mantle is probably dominated by olivine [*Karato and Wu*, 1993]. Next to the microphysical approach to mantle rheology, the inversion of glacial rebound data also gives information on the viscosity of the mantle. Using this approach, *Lambeck et al.* [1998] have found the upper mantle viscosity to be about $3\text{--}4 \times 10^{20}$ Pas. The hotter Archean upper mantle, however, may have had a viscosity several orders of magnitude lower than this figure due to the strong temperature dependence of both diffusion creep and dislocation creep. Furthermore, the temperature dependence of the dislocation creep mechanism as expressed in the activation energy parameter of the rheological flow is higher than for the diffusion creep component. From this one can predict a greater predominance of the dislocation creep component under higher temperature conditions, representative for the early

Earth. This has motivated us to extend our previous work on growth mechanisms of continental roots, based on purely diffusion creep models [*de Smet et al.*, 1998, 1999, 2000a, 2000b; *de Smet*, 1999], with a detailed investigation of more complete viscous rheology including also the rheological effect of dislocation creep flow and sensitivity for the degree of dehydration induced by partial melting.

[4] Nonlinear rheology can greatly enhance the velocity of plumes [*Weinberg and Podladchikov*, 1994; *Larsen et al.*, 1997; *Larsen and Yuen*, 1997; *van Keken*, 1997] relative to a Newtonian rheology case, and can therefore more effectively transport heat up to shallow lithospheric levels. Another important effect of nonlinear rheology is the generation of localized high strain rates, which may result in viscous heating, with a lubricating effect through the temperature dependence of the rheology [*van den Berg and Yuen*, 1997; *Larsen et al.*, 1999]. Combined, these two effects can cause regions of high temperature at shallow depths, which may induce secondary melting and crustal diapirism [*Campbell and Hill*, 1988]. On the other hand, melting lowers the temperature by means of latent heat consumption, and may also increase the viscosity of the residue directly. This is due to the fact that at low degrees of partial melting, water tends to concentrate in the melt phase, effectively drying the residue. Experiments have shown that water has a weakening effect [e.g., *Chopra and Paterson*, 1981], and from these observations, *Karato* [1986] concluded that at low degrees of partial melting, the strength of the residual matrix is increased by melting. This increase of viscosity of the residual depleted peridotite could be as high as a factor of 100 to 180 [*Hirth and Kohlstedt*, 1996]. The importance of this effect for plumes has been ascertained by *Ito et al.* [1999] and *Ito* [2001]. *Karato and Jung* [1998] find that this dehydration effect does not only influence the viscosity, but is also connected to the low seismic velocity and high attenuation in the asthenosphere.

[5] Samples of cratonic lithosphere are found as xenoliths in kimberlite intrusions [*Nixon and Boyd*, 1973] and as larger bodies in some orogenic belts [*Brueckner and Medaris*, 1998; *van Roermund and Drury*, 1998]. It is proposed that many of these

mantle rocks are emplaced into the lithosphere by diapirs from the convecting sublithospheric mantle [*Nicolas*, 1986] in a variety of geodynamic environments [*Green and Gueguen*, 1983; *Nicolas et al.*, 1987; *Fabriès et al.*, 1991]. The PT paths derived from some cratonic peridotites from the Norwegian Western Gneiss Region [*van Roermund and Drury*, 1998; *Drury et al.*, 2001] imply that these rocks were part of diapirs that intruded cratonic lithosphere of Archean to early Proterozoic age (the cooling age of these rocks is 1.7–1.8 Ga, but the Sm-Nd model age indicates a depletion age of 2.5–3.0 Ga). *Drury et al.* [2001] have shown that the PT path of these peridotites is consistent with PT paths of diapiric upwellings calculated from the thermochemical convection models of *de Smet* [1999] and *de Smet et al.* [1999].

[6] In this paper, we present results of numerical modeling experiments which were devised to model the interaction of diapirs with the continental root, and we investigate in particular the sensitivity of the model for the rheological parameterization. We place the models in an Archean setting by prescribing a potential mantle temperature of 1750°C. We determine the effect of varying the rheological flow law from Newtonian diffusion creep only, into a composite law combining both grain size sensitive Newtonian diffusion creep and power law (grain size independent) dislocation creep. Different grain sizes are used to test for varying strengths of the diffusion creep component (dislocation creep is grain size independent). Furthermore, we investigated the effect of dehydration during partial melting. This extends earlier work by *de Smet et al.* [1998, 1999, 2000a, 2000b] and *de Smet* [1999] based on purely Newtonian rheology.

[7] The potential temperature of 1750°C which we use is relatively high and may be representative of the earlier half of the Archean. Parametric cooling models for the Earth of *Richter* [1985] show mantle potential temperatures for the Archean of about 1450 to 1700 centigrade. However, the high MgO contents of Archean komatiites point to higher potential temperatures, up to 1800°C for 2.7 Ga old Belingwe komatiites and even 1900°C for 3.45 Ga old Barberton komatiites [*Nisbet et al.*,

1993]. Melting experiments of *Walter* [1998] show that Archean komatiites can be formed by dry batch melting of pyrolite at pressures of 7 to 10 GPa. Extrapolation along an adiabat of the solidus temperature (using the solidus of *Herzberg and Zhang* [1996]) at these pressures shows that this corresponds to potential temperatures in the range of 1700 to 1800 centigrade. These temperatures probably represent plume temperatures in a cooler mantle. For the current mantle, estimates for the excess temperature of plumes are up to 200 to 250 centigrade [*Herzberg and O'Hara*, 1998]. In a hotter Earth, the temperature controlled viscosity would be lower and therefore also the maximum horizontal temperature variations would be reduced [*McKenzie and Bickle*, 1988; *Nisbet et al.*, 1993] to about 50–150°C [*Nisbet et al.*, 1993], which puts our potential temperature of 1750°C within the range indicated by the komatiites of *Nisbet et al.* [1993]. Some authors have suggested that komatiites may be formed by hydrous melting [*Stone et al.*, 1997] at temperatures only about 100°C higher than present mantle temperatures [*Parman et al.*, 1997]. *Arndt et al.* [1998] however conclude that most komatiites were the product of dry melting. The potential temperature of 1750°C of our models is also consistent with the results of the numerical models of *de Smet et al.* [2000b] which form the starting point of our investigations.

[8] The analysis of structures and microstructures in mantle rocks may provide estimates of the differential stresses and strain rates during high temperature deformation associated with diapir upwelling in a cratonic lithosphere. We use this information to compare our model results to the peridotites from western Norway mentioned above, which are interpreted as a natural example of a Precambrian asthenosphere diapir [*Drury et al.*, 2001].

[9] In the work of *de Smet et al.* [2000b], small-scale diapirs are generated in a self-consistent way in hot upwelling limbs of large-scale (~1000 km) mantle convection cells. Here we take a different approach and zoom in on a smaller region surrounding a single uprising diapir and follow the detailed evolution during its ascent into and within the chemically distinct mantle root.

2. Numerical Model Setup

2.1. Description of the Numerical Model

[10] We have used a 2-D Cartesian thermochemical convection code including partial melting. An extended Boussinesq approach was used assuming infinite Prandtl number, including viscous dissipation, adiabatic compression and latent heat of melting. Partial melting is modeled as an (irreversible) increase in the degree of depletion F , which is defined here as the mass fraction of melt which is extracted from an initially unmelted material control volume of mantle material. Since no material is actually removed in our model, volumes of depleted residual material are somewhat overestimated [*de Smet*, 1999]. Because of the relatively short timescale of the models (<50 Myr), internal heating by the decay of radioactive elements was not included. This model is described by the following nondimensional equations [*de Smet et al.*, 1998]. The energy equation (see Table 1 for explanation of the symbols used):

$$\frac{dT}{dt} - Di(T+T_0)_w = \nabla^2 T + \frac{Di}{Ra} \Phi - \frac{\Delta S}{c_p} \frac{dF}{dt} (T+T_0) \quad (1)$$

The incompressibility condition and the nondimensional momentum equation:

$$\nabla \cdot \vec{u} = 0 \quad (2)$$

$$\nabla [\eta(\nabla \vec{u} + \nabla \vec{u}^T)] - \nabla \Delta p = (RaT + RbF)\hat{z} \quad (3)$$

Evolution of the degree of depletion is described by the following equation:

$$\frac{dF}{dt} = S(P, T, F) \quad (4)$$

The source function S in equation (4) is used to describe the rate of partial melting, applying a simple parameterization of the melting phase diagram of mantle peridotite in terms of a solidus and liquidus. S is defined by means of expressing the differential dF in terms of pressure and temperature differentials as described in more detail in Appendix A of *de Smet et al.* [1998]. We use two different parameterizations of the solidus and the liquidus. The first one has a linear and parallel liquidus and solidus, based on data presented by *Takahashi and Kushiro* [1983] (up to 3.5 GPa, so

Table 1. Symbols of the Energy and Momentum Equations (Equations (1)–(3)), the Transport Equation (4), and the Strain Equation (5)

Symbol	Property	Definition	Value/Unit
c_p	heat capacity at constant pressure		1000/1250 Jkg ⁻¹ K ⁻¹
Di	dissipation number	$(\alpha gh)/c_p$	0.09408
e_{ij}	strain rate tensor	$\partial_j u_i + \partial_i u_j$	s ⁻¹
e	second invariant of the strain rate tensor	$[(1/2)e_{ij}e_{ij}]^{1/2}$	s ⁻¹
F	degree of depletion		
g	acceleration due to gravity		9.8 ms ⁻²
h	length scale		400 × 10 ³ m
Ra	thermal Rayleigh number	$(\rho_0 \alpha \Delta T g h^3)/(\kappa \eta_0)$	1.24 × 10 ⁶
Rb	compositional Rayleigh number	$(\delta \rho g h^3)/(\kappa \eta_0)$	1.42 × 10 ⁶
S	melt productivity function		s ⁻¹
ΔS	entropy change upon full differentiation		300 Jkg ⁻¹ K ⁻¹
t	time		s
T	temperature		°C
T_0	nondimensional surface temperature		273/ΔT
ΔT	temperature scale		1923°C
w	vertical velocity		ms ⁻¹
\hat{z}	unit vector in vertical (downward) direction		
α	thermal expansion coefficient		3 × 10 ⁻⁵ K ⁻¹
ϵ_T	relative amplitude of thermal perturbation	$\delta_T/T(z)$	
η	viscosity		Pas
η_0	reference viscosity		10 ²⁰ Pas
κ	thermal diffusivity		10 ⁻⁶ m ² s ⁻¹
ρ_0	reference density		3416 kgm ⁻³
$\delta \rho$	density difference upon full depletion	$\partial \rho / \partial F$	226 kgm ⁻³
τ_{ij}	deviatoric stress tensor	ηe_{ij}	Pa
τ	second invariant of the deviatoric stress tensor	$[(1/2)\tau_{ij}\tau_{ij}]^{1/2}$	Pa
Φ	viscous dissipation	ηe^2	Jm ⁻³ s ⁻¹

we are extrapolating at higher pressures). The second uses a third-order polynomial parameterization, based on data by *Herzberg and Zhang* [1996]. Our isobaric melting curve, which is based on data presented by *Jaques and Green* [1980], is linear in both cases [*Vlaar and van den Berg*, 1991; *de Smet et al.*, 1998].

[11] Two deformation mechanisms are included in the models: diffusion creep (linear) and dislocation creep (nonlinear). We test models which use the diffusion creep component exclusively (models N1–N3), as well as models with a composite rheology (models C1–C5), combining the diffusion creep and dislocation creep mechanisms (see Tables 2–4 for details). An extra effect also included in some models (models D1–D3) is the effect of dehydration by partial melting. The models will be described in more detail below.

[12] Our composite rheology models combine both the diffusion creep and the dislocation creep mechanisms [see also *van den Berg et al.*, 1993]. Their

combined effect is defined through a superposition of the corresponding strain rates:

$$e_{ij} = e_{ij1} + e_{ij2} = \left[\frac{1}{\eta_1} + \frac{1}{\eta_2} \right] \tau_{ij} \quad (5)$$

Table 2. Symbols of the Equations Describing the Rheology (Equations (7) and (8))^a

Symbol	Property	Value/Unit
A	strain rate prefactor	s ⁻¹
B	effective viscosity prefactor	Pas or Pa ^{3.25} s
b	length of Burgers vector	5 × 10 ⁻¹⁰ m
d	grain size	m
E	activation energy	Jmol ⁻¹
m	grain size exponent	2.5, 0
n	stress exponent	1.0, 3.25
P	pressure	Pa
R	gas constant	8.3144 Jmol ⁻¹ K ⁻¹
T	temperature	K
V	activation volume	m ³ mol ⁻¹
μ	shear modulus	80 × 10 ⁹ Pa
τ	second invariant of deviatoric stress tensor	Pa

^a Values of the viscosity prefactors A and B and grain size and stress exponents m and n are specified in Table 3. Two units are specified for the viscosity prefactor, the first being applicable to diffusion creep, and the second to nonlinear dislocation creep.

Table 3. Parameters for the Different Viscosity Models That are Used^a

JdS	η_{ref} , Pas	P_{ref} , GPa	T_{ref} , °C	E , Jmol ⁻¹	V , m ³ mol ⁻¹	
diff ($k = 1$)	10^{21}	13.39	1750	250×10^3	7.5×10^{-6}	
KW Composite	A_k , s ⁻¹	B_k , Pa ^{3.25} s	n_k	m_k	E_k , Jmol ⁻¹	V_k , m ³ mol ⁻¹
diff ($k = 1$)	7×10^{15}	Table 4	1.0	2.5	270×10^3	6×10^{-6}
disl ($k = 2$)	2.5×10^{20}	1.089×10^{15}	3.25	0	485×10^3	17.5×10^{-6}

^aHere, η_{ref} , P_{ref} and T_{ref} are reference viscosity, pressure and temperature, respectively (other symbols are explained in the caption of Table 2), and are used following *de Smet et al.* [1998, 1999, 2000a, 2000b] and *de Smet* [1999], indicated by JdS. The components of composite rheology are based on data by *Karato and Wu* [1993], indicated by KW, and are chosen to be intermediate between their “wet” and “dry” parameters.

with the subscript 1 indicating diffusion creep and 2 indicating dislocation creep, and the effective viscosity given by

$$\eta = \left[\frac{1}{\eta_1} + \frac{1}{\eta_2} \right]^{-1} \quad (6)$$

The corresponding viscosity components η_k are defined by the dimensional Dorn equation:

$$e_k = A_k \left(\frac{\tau}{\mu} \right)^{n_k} \left(\frac{b}{d} \right)^{m_k} \exp \left[-\frac{E_k + PV_k}{RT} \right], \quad k = 1, 2 \quad (7)$$

We assume a constant grain size d in equation (7) in the diffusion creep component. This is used as a control parameter to distinguish between model cases with different partitioning between the two creep mechanisms.

[13] Equation (7) can be transformed into a viscosity expression [see *van den Berg and Yuen*, 1998]:

$$\eta_k = B_k \exp \left[\frac{E_k + PV_k}{RT} \right] \tau^{1-n_k}, \quad k = 1, 2 \quad (8)$$

For values of n unequal to unity, η_k introduces a nonlinearity through equation (6) in the momentum equation (3) [*van den Berg et al.*, 1993].

[14] Depending on local values of temperature, pressure and shear stress, one of the two creep mechanisms in equation (5) is dominant. We use the grain size as a control parameter for the transition between these domains. The transition stress τ_t at which both mechanisms are equally important for a specific temperature and pressure can be calculated by equating the viscosity components in equation (5), using equation (8), resulting in:

$$\tau_t^{n-1} = \frac{B_2}{B_1} \exp \left[\frac{(E_2 - E_1) + P(V_2 - V_1)}{RT} \right] \quad (9)$$

As shown in Table 3, both $\Delta E = E_2 - E_1$ and $\Delta V = V_2 - V_1$ are positive for the parameters we use. Therefore, the temperature and pressure dependence of the parameter τ_t^{n-1} is similar to the P,T dependence of the viscosity components, with a

Table 4. Models and Their Distinguishing Characteristics^a

Model	Rheology Model	Grain Size, mm	B_1 , Pas	f_{η}	T_{pots} , °C	Sol. + Liq.
N1	JdS	2.8	8.95×10^{11}	1	1800	TK
N2	KW diff.	1.0	8.95×10^{11}	1	1750	HZ
C1	KW	0.5	1.143×10^{10}	1	1750	HZ
C2	KW	1.0	6.465×10^{10}	1	1750	HZ
C3	KW	5.0	3.614×10^{12}	1	1750	HZ
C4	KW	50	1.143×10^{15}	1	1750	HZ
C5	KW	1.0	6.465×10^{10}	1	1750	TK
D1	KW	1.0	6.465×10^{10}	10	1750	HZ
D2	KW	1.0	6.465×10^{10}	50	1750	HZ
D3	KW	1.0	6.465×10^{10}	200	1750	HZ

^aThe entries under “Rheology Model” refer to Table 3. KW indicates both diffusion and dislocation creep components, unless it is specified otherwise (“diff.” for diffusion creep only). JdS indicates a diffusion creep component only. The viscosity prefactor B_k in equation (8) is given for the diffusion creep component, as a function of the grain size. The dislocation creep prefactor B_2 is specified in Table 3, as it is insensitive to grain size. The viscosity depletion factor f_{η} defines the local relative viscosity increase if the local degree of depletion is larger than a threshold, see text for details. The entries under “Sol. + Liq.” refer to the parameterization of the solidus and liquidus that was used, which is either linear (TK, based on data by *Takahashi and Kushiro* [1983]) or third-order polynomial (HZ, based on *Herzberg and Zhang* [1996]).

minimum in the asthenosphere [Karato and Wu, 1993]. The expression (9) indicates that the transition stress decreases for increasing temperature, which implies that for constant pressure non-Newtonian creep becomes more important with increasing temperature. As a consequence of this, the role of dislocation creep in the hotter early Earth must have been greater than today.

[15] The set of equations (2), (3), and (4) was solved using finite element methods and a Predictor-Corrector time integration scheme, described by van den Berg *et al.* [1993]. Picard iteration for the Stokes equation (3) was used to deal with the nonlinearity arising from the nonlinear rheology. The finite element meshes used contain approximately 10^4 triangular (6 point) elements, with element sizes ranging from about 24 km in areas of low flow velocity to approximately 3 km in high flow velocity areas. The degree of depletion F was modeled (equation (4)) using a Lagrangian particle tracer method, using 4×10^5 tracers in a random (uniform) distribution. Fourth-order Runge-Kutta time integration is used to advect the particle tracers with the mantle flow velocity. The transformation of particle tracer field values (the degree of depletion) to finite element Gauss points uses a Particle in Cell algorithm [Hockney and Eastwood, 1988]. We tested two models with the tracer density multiplied by a factor 1.5, which gave no significantly different results, so we are confident that the tracer resolution used (4×10^5) is sufficient. We also tested our thermochemical code using the widely used benchmark given by van Keken *et al.* [1997, case 1a].

[16] The depletion-dependence of the viscosity (dehydration effect) is modeled as a composition dependent viscosity prefactor $f_\eta(F)$. This uses a piecewise linear continuous parameterization: $f_\eta = 1$ for $F < 0.005$. For $F > 0.05$ $f_\eta = 10$ (model D1 in Table 3), 50 (model D2), or 200 (model D3). In the intermediate interval $0.005 < F < 0.05$ f_η is a linear function of F , continuous at the interval boundaries. The small width of the transition interval from $f_\eta = 1$ to $f_\eta = 10$, 50 or 200 corresponds to the fact that most water is expelled already at low degrees of melting [Karato and Jung, 1998, Figure 3]. The choice of the magnitude of this prefactor is based

on two observations. The first is experimental results by Hirth and Kohlstedt [1996], indicating a viscosity increase by a factor of 100 to 180 upon dehydration. This gives an upper bound factor of 200. The second observation is evidence for rehydration found in studies of craton xenoliths [Harte, 1983]. Since rehydration would lower the viscosity again, we have used two, admittedly arbitrary, lower bound values of 10 and 50. The rheological parameters which are used are presented in Tables 3 and 4, and the labeling of the different model cases is defined in Table 4.

[17] For models C1–C5 and D1–D3 (composite rheology cases), we specified the parameters in equation (7). We used intermediate values between the wet and dry parameters of Karato and Wu [1993, p. 773], since they conclude that “the rheology of the . . . subcontinental upper mantle is between that of dry (water-free) and wet (water-saturated) olivine,” based on the water content of basalts, infrared spectroscopy of mantle minerals, laboratory studies of water solubility in olivine and observations of the electrical conductivity of the suboceanic upper mantle. Each model run has a constant grain size, which is varied between the models from 0.5 to 5 mm. This results in the effective prefactors B_k of equation (8), the values of which are specified in Tables 3 and 4. For models N1–N2 (Newtonian rheology), we specified a reference viscosity η_{ref} at a reference pressure P_{ref} and temperature T_{ref} , and activation energy and volume, following de Smet *et al.* [2000a], to allow direct comparison of the results.

[18] The density of mantle material is related to the degree of depletion F [Jordan, 1979]. In the buoyancy term of the Stokes equation (3), we use a linearized parameterization of the composition dependent density [Vlaar and van den Berg, 1991], and the coefficient $\partial\rho/\partial F$ enters the compositional Rayleigh number Rb , in the momentum equation (3) [see also de Smet *et al.*, 1998, 2000b]. We assume all melt to be removed instantaneously to shallower or surface levels, where it can no longer play a role in the development of the diapirs. Because of this assumption, we neglect the buoyancy effect of melt retention, which leads to an underestimate of the buoyancy term [e.g.,

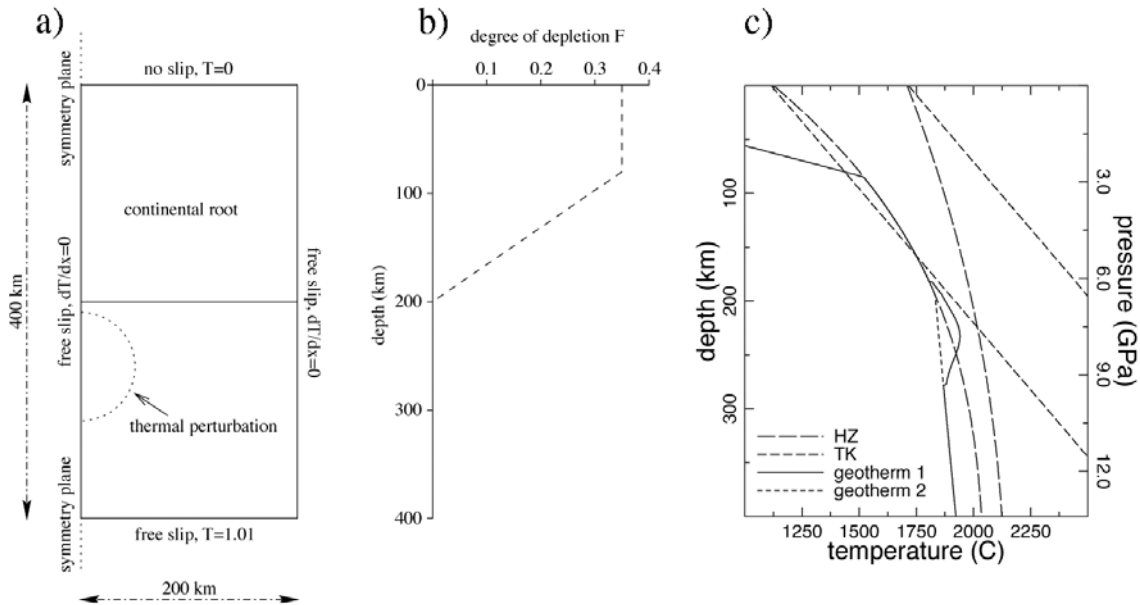


Figure 1. Model setup is shown in Figure 1a. The rectangular domain is 200×400 km and has free slip boundary conditions except for a no slip to boundary. A symmetry plane is present at $x = 0$. Next to the representation of the computational domain, the initial degree of depletion profile is plotted in Figure 1b. The solidus and liquidus parameterizations used are shown in Figure 1c (TK: linear, based on *Takahashi and Kushiro* [1983]; HZ: third-order polynomial, based on *Herzberg and Zhang* [1996]) with the most commonly used perturbed (geotherm 1) and background (geotherm 2) initial geotherms, see text for details.

Scott and Stevenson, 1989; *Buck and Su*, 1989; *Jha et al.*, 1994]. This partly cancels the overestimation of the volume of depleted residue mentioned above.

[19] For most of the models, we use a third-order parameterization of the solidus and liquidus in the melting phase diagram of mantle peridotite [*Herzberg and Zhang*, 1996], which is an improved version of the first-order approximation (based on *Takahashi and Kushiro* [1983]), that is used in models N1 and C5 only. The former is a more accurate description of the solidus and liquidus, especially for melting at depths greater than 100 km.

[20] Since we are working in a 2-D Cartesian geometry, the structures we are modeling can be extended in the third dimension, and we are in fact dealing with a horizontal cylinder rather than a more or less spherical diapir. In an axisymmetric geometry, diapir penetration along the axis of symmetry is easier than in 2-D Cartesian geometry, and subsequent spreading of the diapir head will be more pronounced in 2-D Cartesian geometry than in an axisymmetric geometry. However, we do not

expect these differences to dominate the results of our model experiments.

2.2. Model Geometry and Initial and Boundary Conditions

[21] We have adopted a 200×400 km spatial domain with a symmetry condition on the vertical boundaries shown in Figure 1. Because of the limited aspect ratio of the domain, we have ensured by running tests with aspect ratios up to 6 times higher that possible effects of the right hand side vertical boundary play no significant role in the results of the modeling experiments. We define an initial degree of depletion profile starting with $F = 0$ from 400 to 200 km depth and increasing linearly to $F = 0.35$ from 200 to 80 km depth, keeping this value up to the surface (see Figure 1). This is a reasonable approximation of the continental roots as formed by the long term evolution models of *de Smet et al.* [1999, 2000b].

[22] As an initial geotherm, we use the minimum value of the following three functions; (1) an adiabat (potential temperature 1750°C), (2) a linear

profile from 0°C at the surface to the adiabat at 100 km depth, with a gradient $\partial T/\partial z = 17.9$ K/km, and (3) the solidus of mantle peridotite (see Figure 1).

[23] The mantle diapir which is the subject of investigation is initiated here by adding a Gaussian circular shaped thermal perturbation to the local background temperature. We use a perturbation with a radius (defined as the 2σ (2 standard deviations) distance from the maximum) of 48 km at 230 km depth and $x = 0$ with an amplitude ϵ_T of 5% of the local background temperature (approximately 95°C), see also Figure 1. This is in accordance with thermal anomalies found by *de Smet et al.* [2000b] in mantle convection models of continental root growth. In their model, a thermal perturbation originating from deeper levels of the mantle crosses the solidus, starts melting and accelerates due to increasing depletion related buoyancy. Since these original models by *de Smet et al.* [2000b] employ a purely Newtonian rheology, the self-consistent generation of these plumes in a composite rheology and thus the choice of our initial condition is an extrapolation. The results are sensitive to the amplitude and radius of the initial temperature perturbation (as will be illustrated in Figures 14 and 15 below). In case the upper part of the initial perturbation is above the solidus temperature, the local degree of depletion is adjusted accordingly, creating an initial depletion.

[24] All boundaries of the model are impermeable. The top boundary has a no slip condition, the others are free slip. Thermal boundary conditions are zero centigrade temperature at the top boundary, 1923°C at the bottom (consistent with the potential temperature of 1750°C), and insulating vertical boundaries.

[25] In comparing the different results, it should be kept in mind that in all cases the same initial condition for the starting diapir is used (apart from model N1, which has the same relative perturbation of the temperature field but a higher potential temperature).

2.3. Model Parameters

[26] Detailed parameters of the different models are specified in Tables 3 and 4. Further physical

parameters are given in Tables 1 and 2. We note that two different values of the specific heat c_p have been used. The lower value of $1000 \text{ J kg}^{-1} \text{ K}^{-1}$ is used to compare our results directly to previous results from *de Smet et al.* [1998], model N1 in section 3.2. In all other cases we use a constant $c_p = 1250 \text{ J kg}^{-1} \text{ K}^{-1}$, based on data of *Fei et al.* [1991], resulting in a slightly reduced adiabatic gradient. We also consider two values of the potential temperature characterizing the adiabats used in the initial background temperature in our models. In the comparison case N1 we use a higher value of 1800 centigrade representative for the results of *de Smet et al.* [1998]. In all other models a reduced potential temperature $T_p = 1750$ centigrade is used. This lower temperature would cause a lower degree of melting. However, this is countered by the use of the improved third order parameterization of solidus and liquidus (see section 2.1), which allows melting at depths greater than 200 km at lower temperatures than the linear parameterization.

3. Results of Numerical Modeling

[27] In this section we present the results of our numerical models. First the results of linear rheology models N1 and N2 will be presented, followed by the composite rheology models C1–C5. For each of these, snapshots of temperature, composition, and viscosity and profiles of the composition and the temperature are shown. The transition between the two viscosity components will be described, illustrated by viscosity ratio plots and deformation maps. Subsequently, the effect of dehydration will be shown in the results of models D1–D3, again presenting snapshots and profiles of temperature and compositions and snapshots of viscosity. Finally, ascent velocities for the diapirs and, in more detail, P,T paths and stress and strain rate histories for individual tracers will be presented.

3.1. General Characteristics

[28] In general terms (and ignoring timescales), the development of all diapir models is compa-

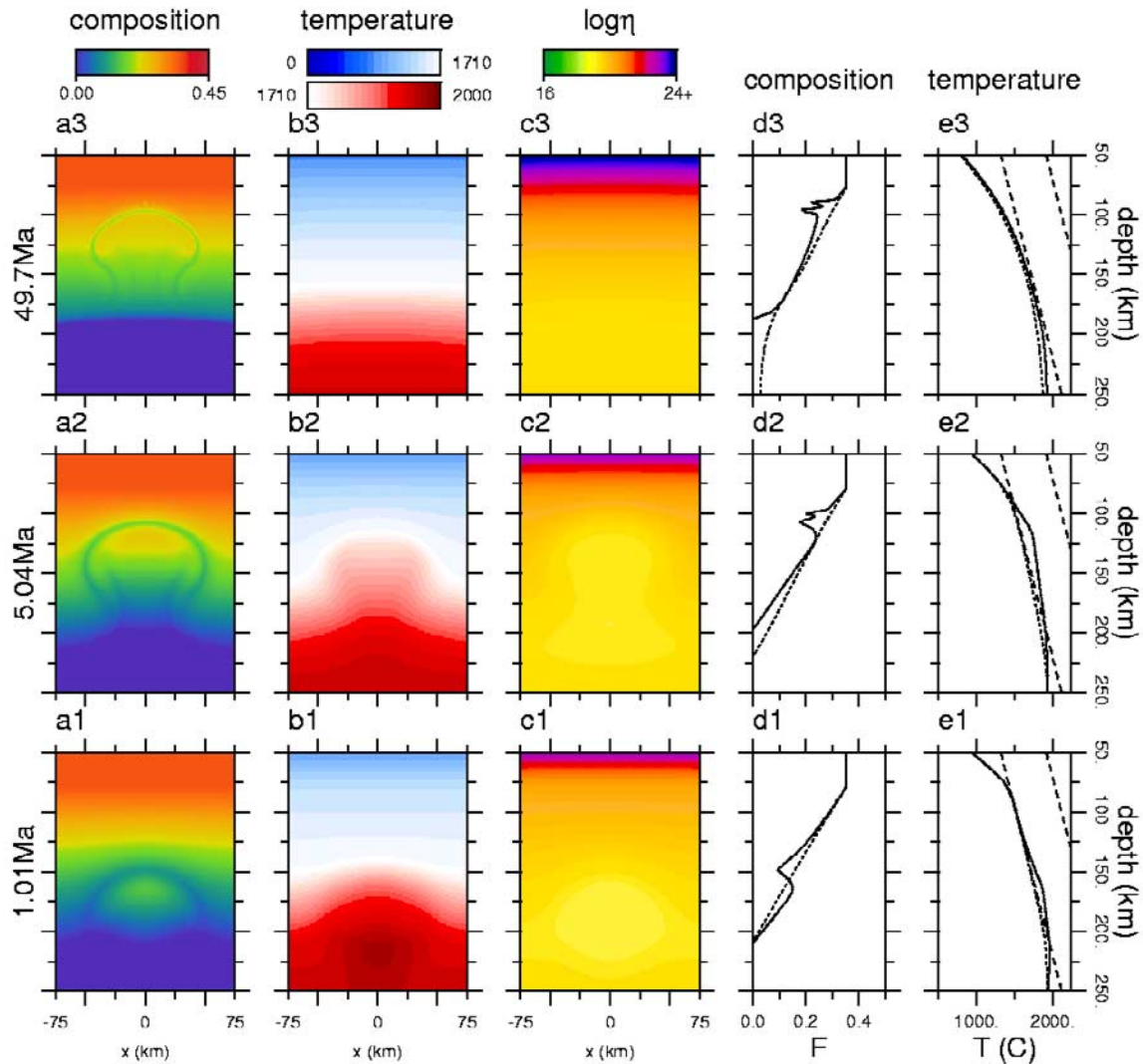


Figure 2. Model N1: Newtonian rheology only. Frames a1–3 show snapshots of the composition (or degree of depletion) field at 1.01 Myr, 5.04 Myr and 49.7 Myr after the start of the model run. The dimensions of the model are 400×400 km, but only a part of the domain is shown ($[x, y] = [-75-75, 50-250]$ km). Snapshots of the temperature field are presented in frames b1–3, and of the viscosity field in c1–3. Frames d1–3 and e1–3 show profiles of the composition and the temperature, respectively. The solid lines are profiles at $x = 0$ km, which is the middle of the model, and dashed lines are profiles at $x = 200$ km, which are relatively undisturbed. The long-dashed lines of frames e1–3 are the solidus and liquidus.

rable. (This is illustrated in Figures 2–7 and 10–12, which show a zoom-in window of part of the computational domain around the rising diapir. Note that the computational domain has been enlarged by adding the region $x < 0$ by symmetric extension around $x = 0$. Snapshots are shown of a rising diapir with time increasing upward labeled in the left hand column. Snapshots of degree of depletion, temperature and viscosity as well as profiles of the degree of depletion and

temperature are shown in different columns a through e.)

[29] In each case, we see melting taking place by the formation of depleted material visible in frames a1–3. As the diapir rises, the highly depleted material at the top of the diapir head is swept aside, causing a decrease in the magnitude of the depletion peak visible in the composition profiles in frames d1–3 of these figures. The narrow band

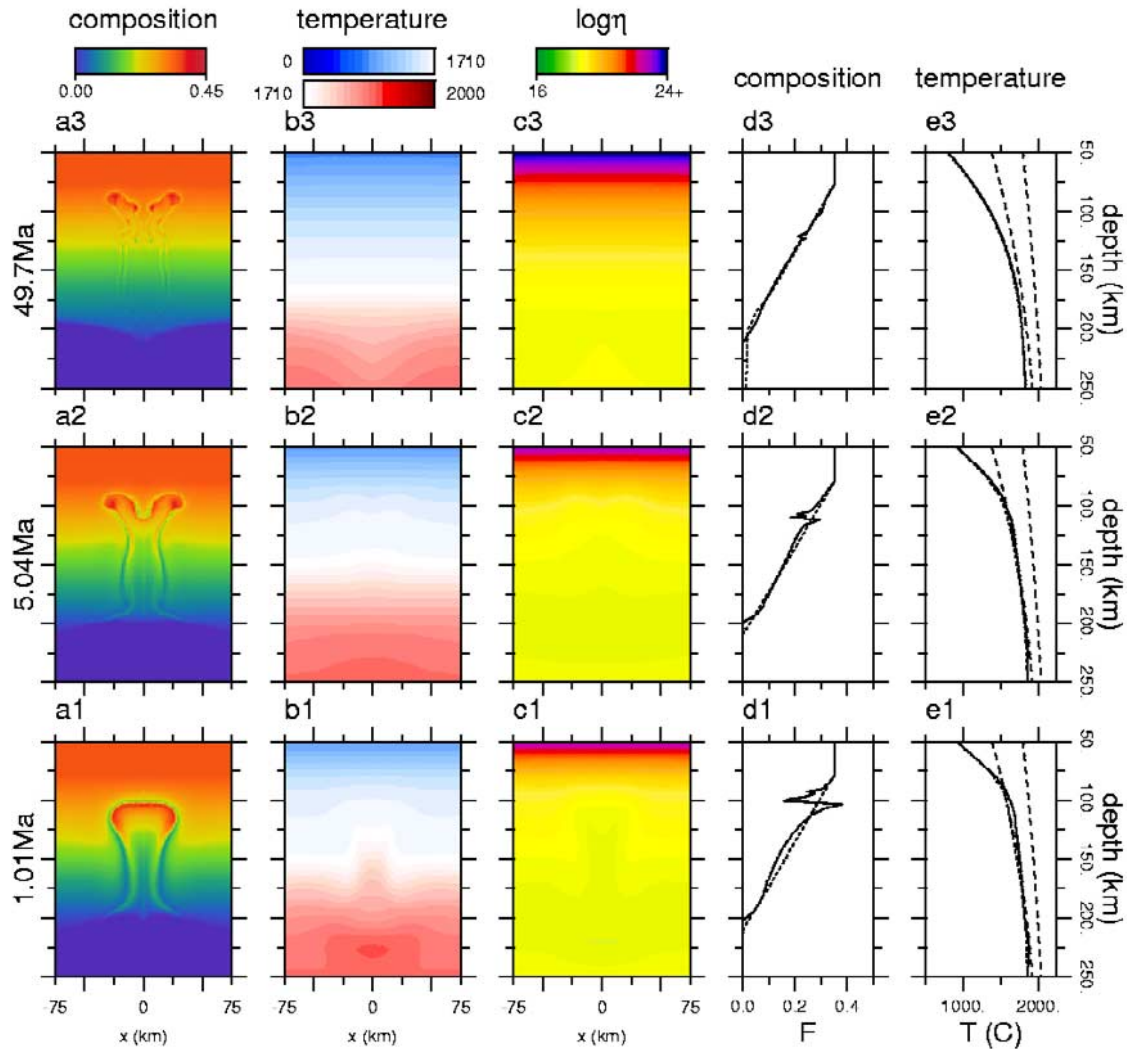


Figure 3. Model N2: Newtonian rheology. Only a part of the domain is shown ($[x, y] = [-75-75, 50-50]$ km). Frames a1–4 show the composition field and frames b1–3 show the temperature field at 1.01 Myr, 5.04 Myr and 49.7 Myr after the start of the model run. Snapshots of the viscosity field are presented in frames c1–3. Profiles of composition and temperature are presented in frames d1–3 and e1–3, respectively. For an explanation of line types, see caption of Figure 2.

of low depletion initially surrounding the diapir head is stretched and thinned, reducing its visibility. The temperature snapshots show a decline of the thermal perturbation back to the background temperature field.

3.2. Linear Rheology Results

[30] Results of a case with linear rheology model N1 are presented in Figure 2. The degree of depletion snapshots (frames a1–3) show the diapir developing a clear mushroom shape of some 100 km in

diameter, quite similar to the diapir examined by *de Smet et al.* [1998], which developed self-consistently in a convecting upper mantle model. Corresponding temperature snapshots are shown in Figure 2b1–3. The figures illustrate the development of the decaying temperature anomaly of the hot diapir. The final snapshot at approximately 50 Myr shows the thermal anomaly has disappeared. The viscosity snapshots (c1–3) show a relatively uniform field in a large part of the domain, with a somewhat lower viscosity down to about 10^{19} Pas inside the diapir resulting from the thermal pertur-

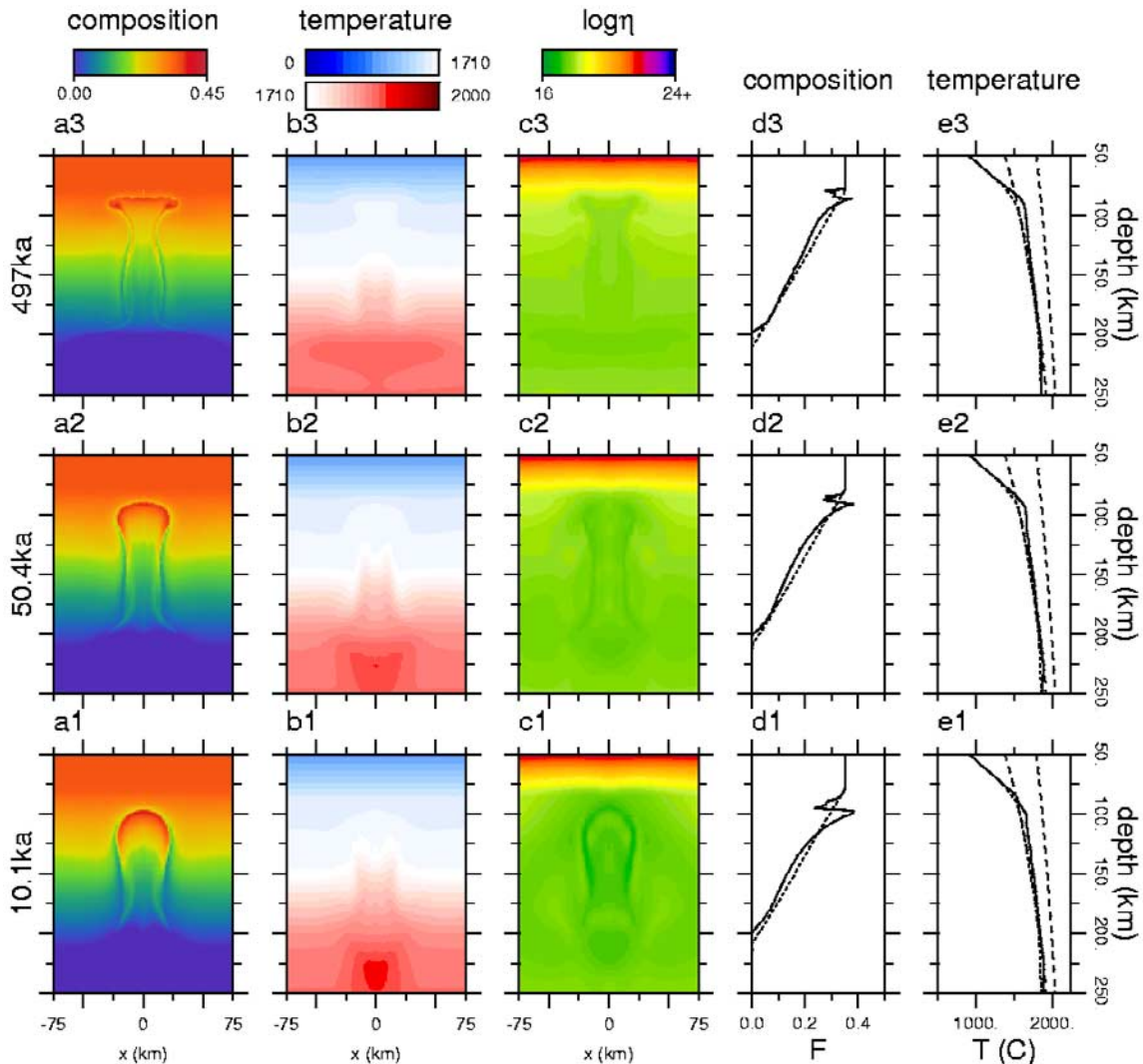


Figure 4. Model C1: Composite rheology. Only a part of the domain is shown ($[x, y] = [-75-75, 50-250]$ km). Frames a1–3 show the composition field and frames b1–3 show the temperature field at 10.1 ka, 50.4 ka and 497 ka after the start of the model run. Snapshots of the viscosity field are presented in frames c1–3. Profiles of composition and temperature are presented in frames d1–3 and e1–3, respectively. For an explanation of line types, see caption of Figure 2.

bation. The degree of depletion in the melting diapir reaches a value of about 0.25.

[31] Vertical profiles of the composition (degree of depletion F) and temperature are shown in frames d1–3 and e1–3, respectively. The solid lines corresponding to centerline profiles at $x = 0$ reveal the magnitude of the rising perturbation of the composition and temperature constituting the diapir, with respect to the background model which is represented by the dotted curves, corresponding to vertical profiles at $x = 200$ km, which is a relatively undisturbed part of the model. The dashed curves in

Figure 2e1–3 showing the Takahashi and Kushiro type solidus and liquidus used in the model illustrate the changing melt conditions as the diapir rises through the mantle. The results reproduce closely the previous results obtained by *de Smet et al.* [1998] for a larger model where diapirs of a similar scale are generated in a self-consistent way in upwelling lines of large-scale mantle convection cells.

[32] Figure 3 shows the results of model N2 with slightly different rheology parameters (following *Karato and Wu* [1993], see Table 3, Newtonian component only), and somewhat modified values

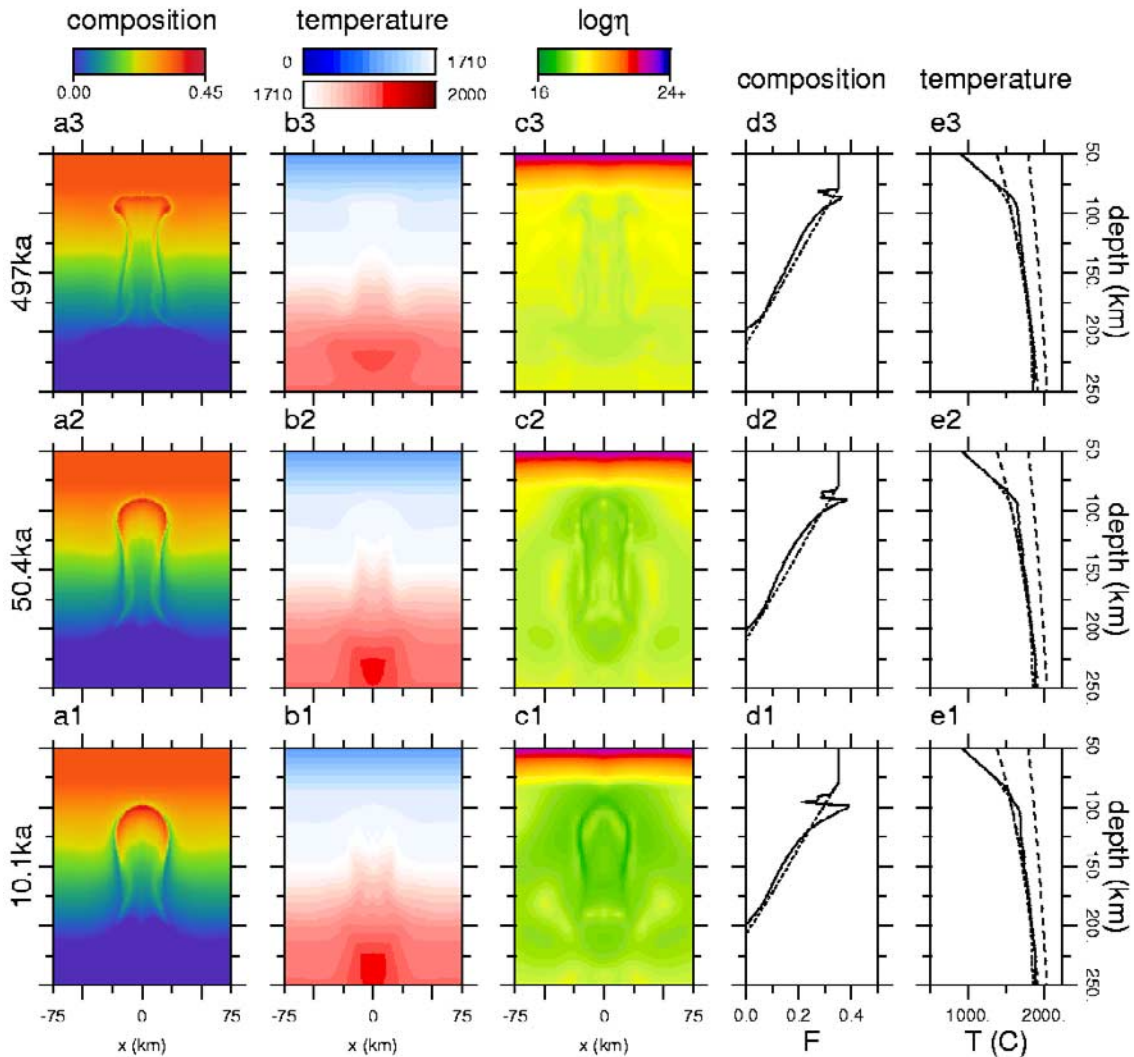


Figure 5. Model C2: Composite rheology. Only a part of the domain is shown ($[x, y] = [-75-75, 50-250]$ km). Frames a1–3 show the composition field and frames b1–3 show the temperature field at 10.1 ka, 50.4 ka, 497 ka after the start of the model run. Snapshots of the viscosity field are presented in frames c1–3. Profiles of composition and temperature are presented in frames d1–3 and e1–3, respectively. For an explanation of line types, see caption of Figure 2.

for the potential temperature (1750°C) and c_p ($1250 \text{ J kg}^{-1} \text{ K}^{-1}$, see Table 4). The modified rheology parameters result in a lower viscosity than in model N1, with a minimum value of about 2.8×10^{18} Pas (frames c1–3), resulting in faster diapir ascent and much stronger deformation of the diapir head (see frames a1–3). The head rises to about 85 km depth in less than 5 million years, and is split in two by colder root material. In spite of the reduced initial temperature compared to model

N1 as shown in frames e1–3, a higher degree of depletion is attained with a maximum of 0.38 due to the faster ascent.

3.3. Composite Rheology Results: Grain Size Variation

[33] Models C1, C2, C3 and C4 have a composite rheology (see Tables 3 and 4) with a grain size parameter of 0.5 mm, 1.0 mm, 5.0 and 50 mm respectively. Results of these models are

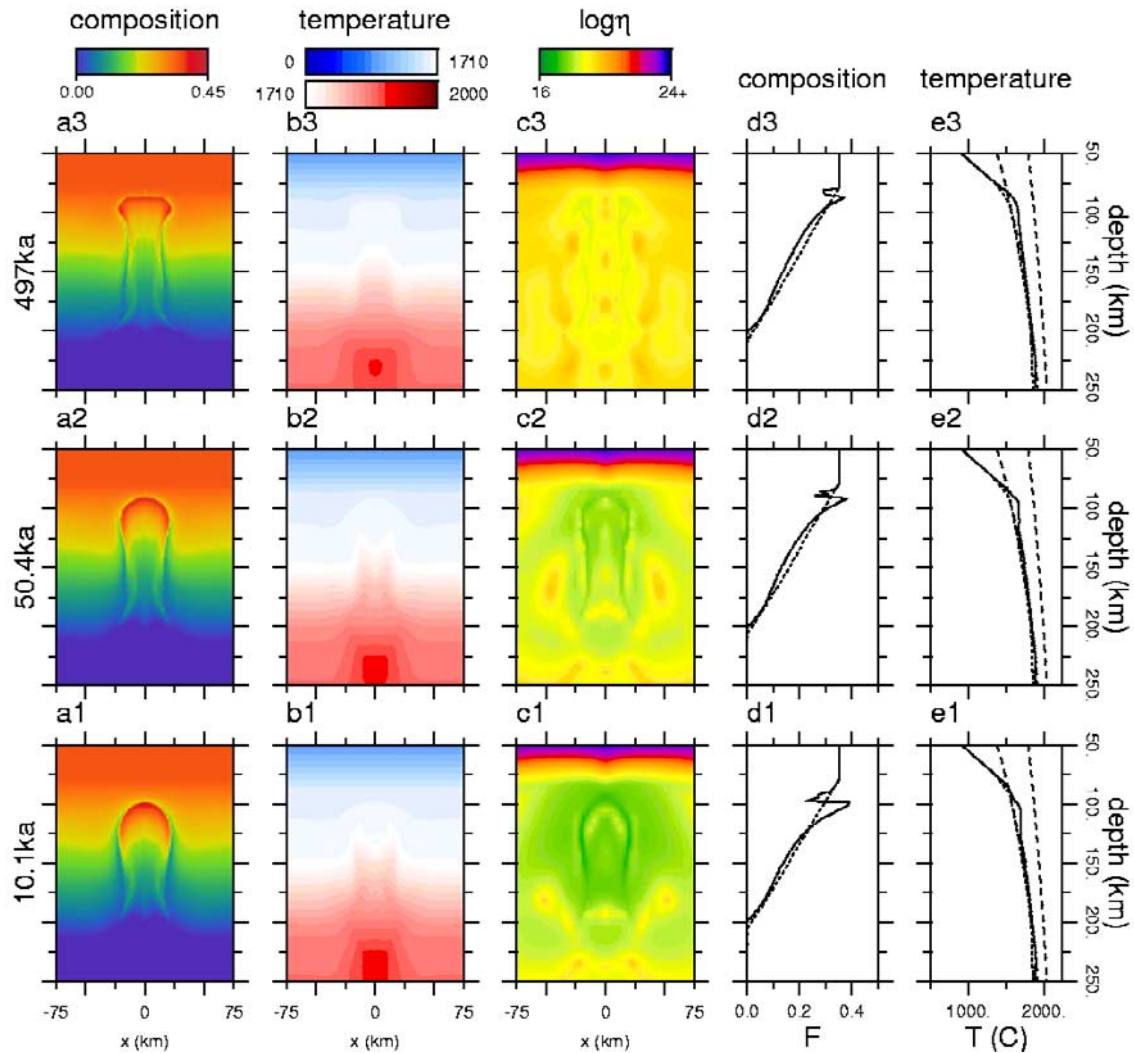


Figure 6. Model C3: Composite rheology. Only a part of the domain is shown ($[x, y] = [-75-75, 50-250]$ km). Frames a1–3 show the composition field and frames b1–3 show the temperature field at 10.1 ka, 50.4 ka and 497 ka after the start of the model run. Snapshots of the viscosity field are presented in frames c1–3. Profiles of composition and temperature are presented in frames d1–3 and e1–3, respectively. For an explanation of line types, see caption of Figure 2.

presented in Figures 4, 5, 6 and 7, respectively. Note that snapshot times are different from those in Figure 2. The development of the degree of depletion field is also shown in Animation 1. Frames a1–3 show the development of the degree of depletion field, which reaches a value of about 0.38 in the diapir head. Initially the diapir shows very rapid ascent (1500 m/yr), but strongly decelerates, dropping below 1 cm/yr after 150 ka. These four models show only slightly different ascent velocities (slower for larger grain size), which will be discussed in

section 3.7. The viscosity field (frames c1–3) shows large local variations because of the strain rate dependence, showing a minimum of comparable magnitude (6.7×10^{16} Pas to 8.5×10^{16} Pas for models C1 to C4) in each case. A horseshoe shaped zone characterized by high strain rate and (through the strain rate dependence of dislocation creep) low viscosity forms around the diapir facilitating the rise of the diapir with a much higher velocity compared to the Newtonian model. While minimum viscosities are quite similar for the different cases C1 to C4, the mantle

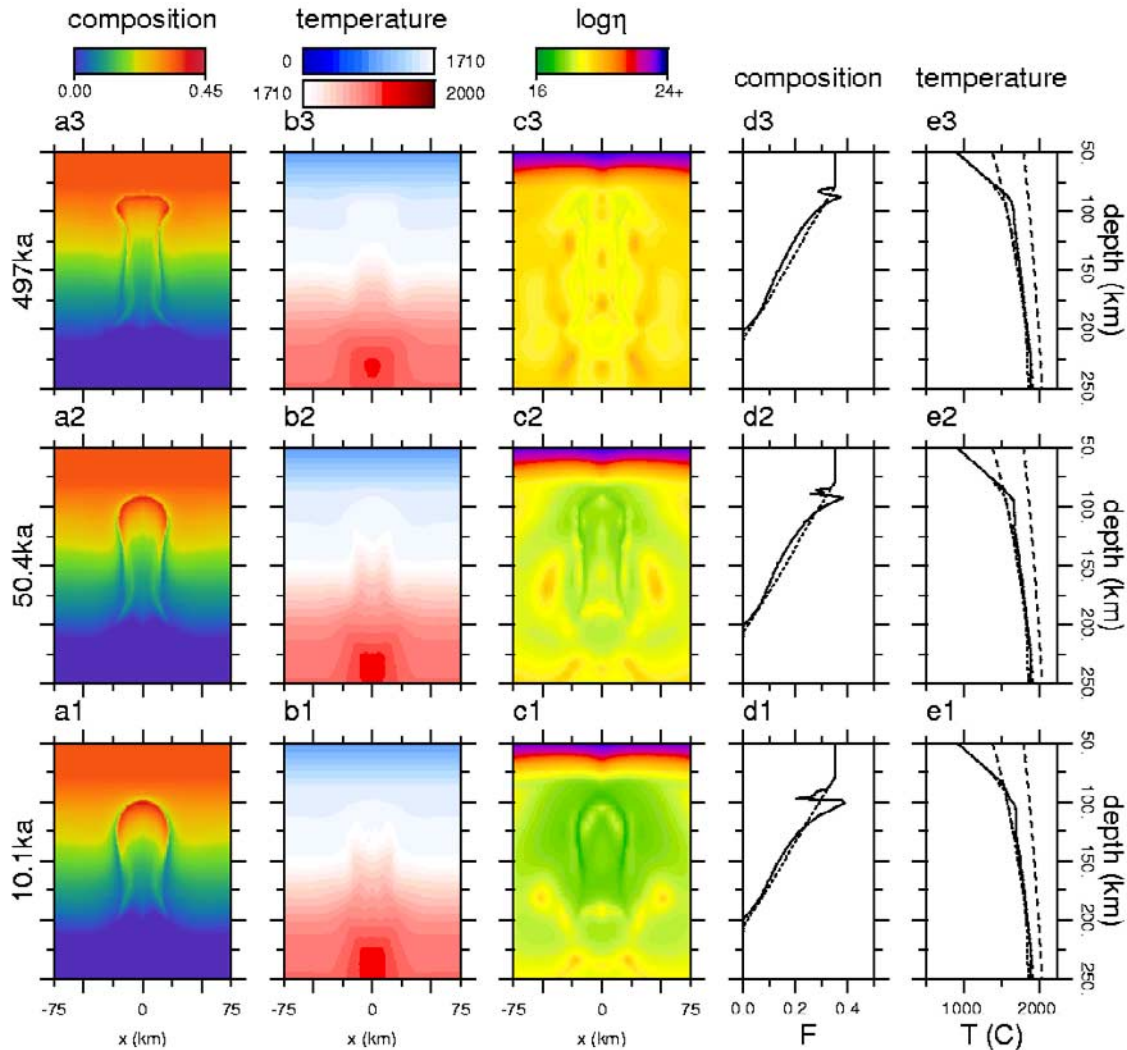


Figure 7. Model C4: Composite rheology. Only a part of the domain is shown ($[x, y] = [-75-75, 50-250]$ km). Frames a1–3 show the composition field and frames b1–3 show the temperature field at 10.1 ka, 50.4 ka, 497 ka after the start of the model run. Snapshots of the viscosity field are presented in frames c1–3. Profiles of composition and temperature are presented in frames d1–3 and e1–3, respectively. For an explanation of line types, see caption of Figure 2.

and root material surrounding the diapir shows much higher viscosities for larger grain sizes, since the strain rate in these regions is much smaller than in the narrow low viscosity region directly bordering the diapiric head. The fact that characteristic timescales in these four models are quite similar despite the large variation in grain size and consequently the relative importance of the deformation mechanisms shows a self-regulating mechanism to be operative, producing similar viscosity minima and corresponding velocities and ascent times. Even for the smallest

grain size, stresses locally become sufficiently large to become greater than the transition stress and the dislocation creep mechanism becomes dominant. As stresses drop during the ascent, they get close to the transition stress and the diffusion creep mechanism starts to play a more important role.

[34] Here we have to keep in mind that the models are based on a constant grain size and taking into account grain size variation may change this conclusion [Kameyama *et al.*,

1997]. However, experimental results of *de Bresser et al.* [1998, 2001] indicate that significant weakening by grain size reduction can only take place if the grain size reduction is [*de Bresser et al.*, 2001, p. 28] “caused by a process other than dynamic recrystallization.” *de Bresser et al.* [2001, p. 28] do find that the effect of temperature on recrystallized grain size “cannot be neglected a priori.” In the upper mantle the grain size is expected to be controlled either by dynamic recrystallization [*Karato et al.*, 1980; *Karato and Wu*, 1993] or by secondary phase content [*Drury and Fitz Gerald*, 1998, Figure 11.7f]. For dynamic recrystallization the grain size will depend strongly on the stress (smaller grains at higher stress) with a weaker dependence on temperature (smaller grains at higher temperature) and water content (larger grains at higher water content) [*Karato et al.*, 1980; *Ross et al.*, 1980; *van der Wal et al.*, 1993; *de Bresser et al.*, 1998, 2001; *Jung and Karato*, 2001]. At low stress and high temperature the olivine grain size will be controlled by secondary phase size and content [*Drury and Fitz Gerald*, 1998]. In this case the grain size will depend strongly on the degree of depletion, which determines the second phase content. This is a subject of continuing research.

[35] Model C1 (composite rheology after *Karato and Wu* [1993], see Tables 3 and 4) was calculated also using the linear parameterization of solidus and liquidus based on *Takahashi and Kushiro* [1983] (which was also used in model N1) instead of the third-order polynomial parameterization based on *Herzberg and Zhang* [1996] (also used in models N2 and C1-4, see also section 2.1 and Figure 1), which gives us model C5. Because of the linear parameterization, which has considerably higher solidus and liquidus temperatures at greater depths (>100 km), the thermal perturbation which should have developed into a diapir does not penetrate the root at all, and produces very little melt. This result underlines the key role of compositional differentiation. The generation of depleted peridotite causes compositional buoyancy which further drives the upward movement of the diapir. In this way it provides a self-accelerating mecha-

nism which allows mantle diapirs to penetrate an existing continental root.

3.4. Viscosity Component Ratios

[36] The relative importance of the two deformation mechanisms which are included in the composite rheology is illustrated by Figure 8, showing the logarithmic ratio of dislocation creep viscosity over diffusion creep viscosity (both defined in equation (8)) for the entire domain (dashed rectangle shows the zoom-in part shown in Figures 4–7) for models C1, C2, C3 and C4, respectively. Note that the mechanism which has the lowest effective viscosity for the local conditions dominates the local deformation. Minima of the viscosity ratio η_2/η_1 are visible in the diapir and its surroundings. These are produced by the high stresses and strain rates at these locations which cause a reduction of the non-linear dislocation creep viscosity component, resulting in a decrease of the effective viscosity (equation (6)). The increase of this ratio with time for each model illustrates the decrease of strain rates during the diapir ascent, which causes strain rate dependent dislocation creep viscosities to increase. Another feature of this figure is the greater dominance of dislocation creep for larger grain sizes, which is the result of the grain size dependence of the diffusion creep component (higher viscosity for larger grains). We note here that the grain size dependence of our rheological models characterized by constant grain size represents a simplified version of the stress, temperature, water content and secondary phase dependent grain size in nature [*Karato et al.*, 1980; *van der Wal et al.*, 1993; *de Bresser et al.*, 2001; *Drury and Fitz Gerald*, 1998; *Jung and Karato*, 2001]. A constant grain size model may indeed be a good approximation for the undepleted sublithospheric mantle [*Drury and Fitz Gerald*, 1998], although, in the lithosphere grain size variation with depth would occur related to variations in the degree of depletion. *Kameyama et al.* [1997] and *Braun et al.* [1999] have investigated 1-D models including dynamic grain size evolution exhibiting strong localization. However, the rheological effect of dynamic

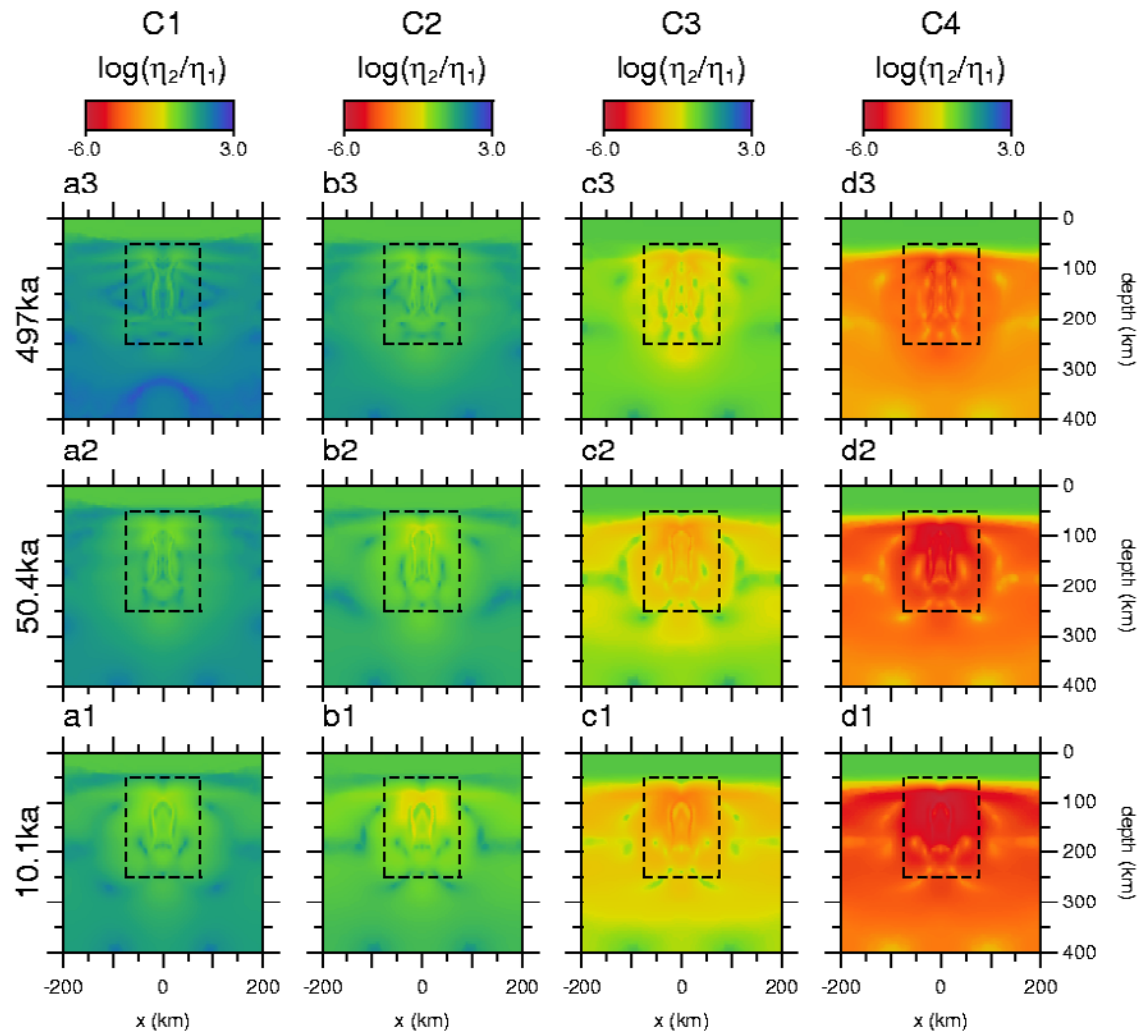


Figure 8. Models C1, C2, C3, C4: Composite rheology. The dashed square indicates the region which is shown in Figures 4–6. The logarithmic ratio of non-Newtonian to Newtonian component viscosity of the composite rheology at 10.1 ka, 50.4 ka and 497 ka is presented in frames a1–3 for model C1, frames b1–3 for model C2, frames c1–3 for model C3 and frames d1–3 for model C4.

recrystallization remains uncertain and controversial [Rutter and Brodie, 1988; de Bresser et al., 1998, 2001]. Including dynamic grain size evolution in 2-D models is a subject for further research both in terms of the modeling and the microphysical aspects.

3.5. Deformation Maps

[37] In Figure 9, the logarithmic transition stress τ_t defined in equation (9) is contoured as a function of temperature and pressure (depth), for four different values of the grain size corresponding to models C1–4. Geotherms at $x = 0$ (through the

diapir) and $x = 200$ km (undisturbed) are included as well. At stresses higher than τ_t , dislocation creep is dominant, at lower stress diffusion creep prevails. The variation of the grain size directly controls the diffusion component of the viscosity, resulting in different magnitudes of the transition stress for equal P,T-conditions. As the figure clearly shows, a larger grain size decreases the transition stress τ_t from about 1 MPa in the region of the diapir, as illustrated by the geotherms included in the figure, for a grain size of 0.5 mm to less than 10^4 Pa for a grain size of 50 mm. These features relate to the viscosity ratios which are presented in Figure 8. For model C1 with a 0.5

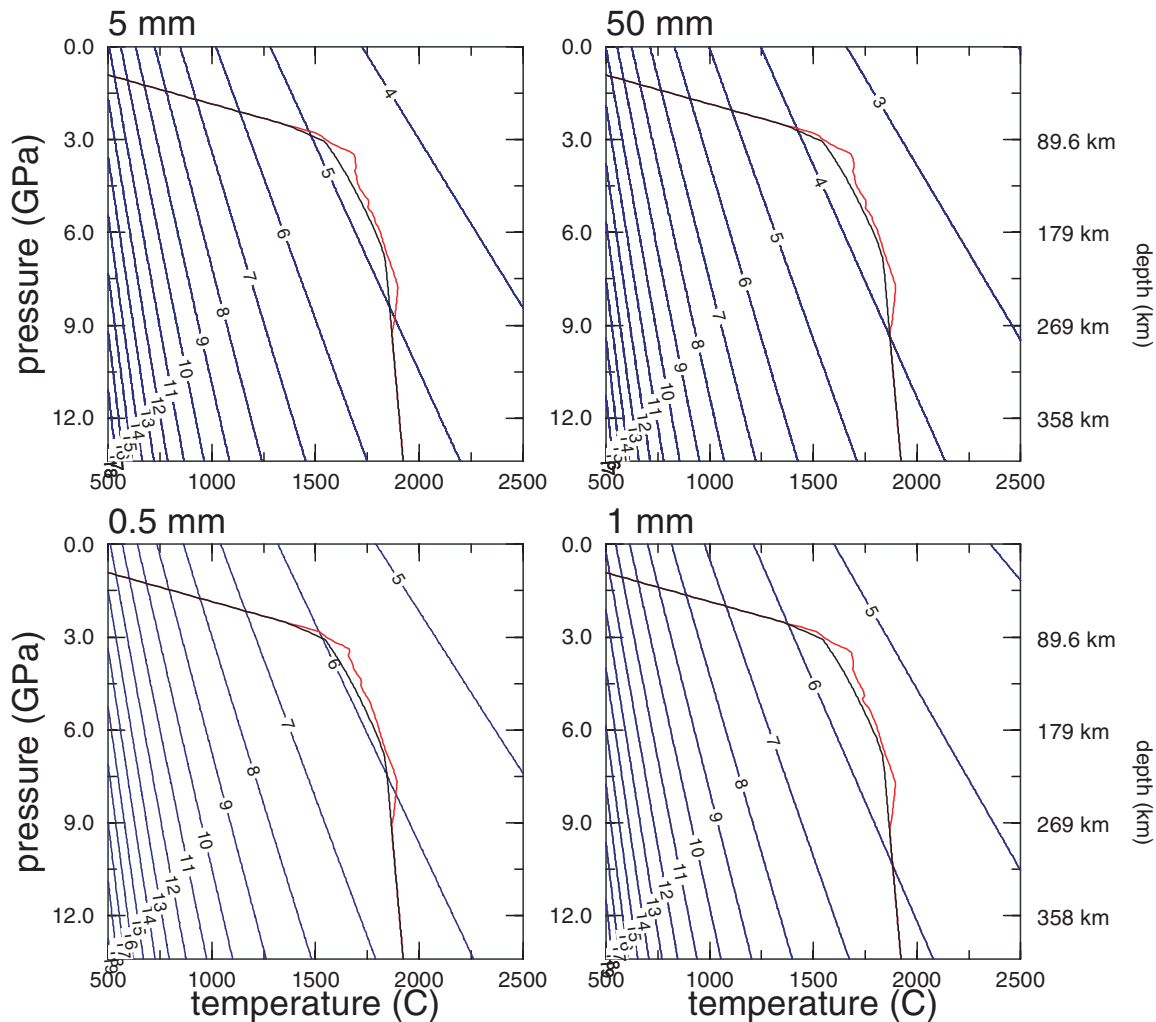


Figure 9. Models C1, C2, C3, C4: Composite rheology. Deformation maps are shown for the composite rheology models used (0.5 mm, 1.0 mm, 5.0 mm and 50 mm grain size) and geotherms at $x = 0$ (diapir center, red lines) and $x = 200$ km (undisturbed background, black lines) at $t = 10.1$ ka. Contours show the (logarithmic) stress τ_t at which dislocation creep viscosity is equal to diffusion creep viscosity. At a higher stress than τ_t , dislocation creep is the dominant deformation mechanism.

mm grain size, stresses in the diapiric region are approximately of the same magnitude as the transition stress, causing the viscosity ratio of the two creep components to be roughly 1. For increasingly larger grain sizes in models C2–4, the transition stress drops more and more below the actual stress levels observed in the diapirs, and the viscosity ratio becomes lower, down to about 10^{-6} for model C4 with grain size of 50 mm.

3.6. Dehydration and Viscosity

[38] The effect of dehydration due to partial melting on the rheology is investigated in models D1–3.

The dehydration prefactor in the viscosity applied in these models is used irrespective of the dominant creep mechanism. This is justified by experimental results [Karato, 1986; Mei and Kohlstedt, 2000a, 2000b], indicating similar increases in creep velocity due to hydration for both diffusion creep and dislocation creep.

[39] In model D1, the viscosity is multiplied by a factor 10 when the degree of depletion becomes higher than a threshold value, as described in the model section (2.1). The results of this viscosity prefactor are illustrated in Figure 10. Frames c1–3 show the viscosity

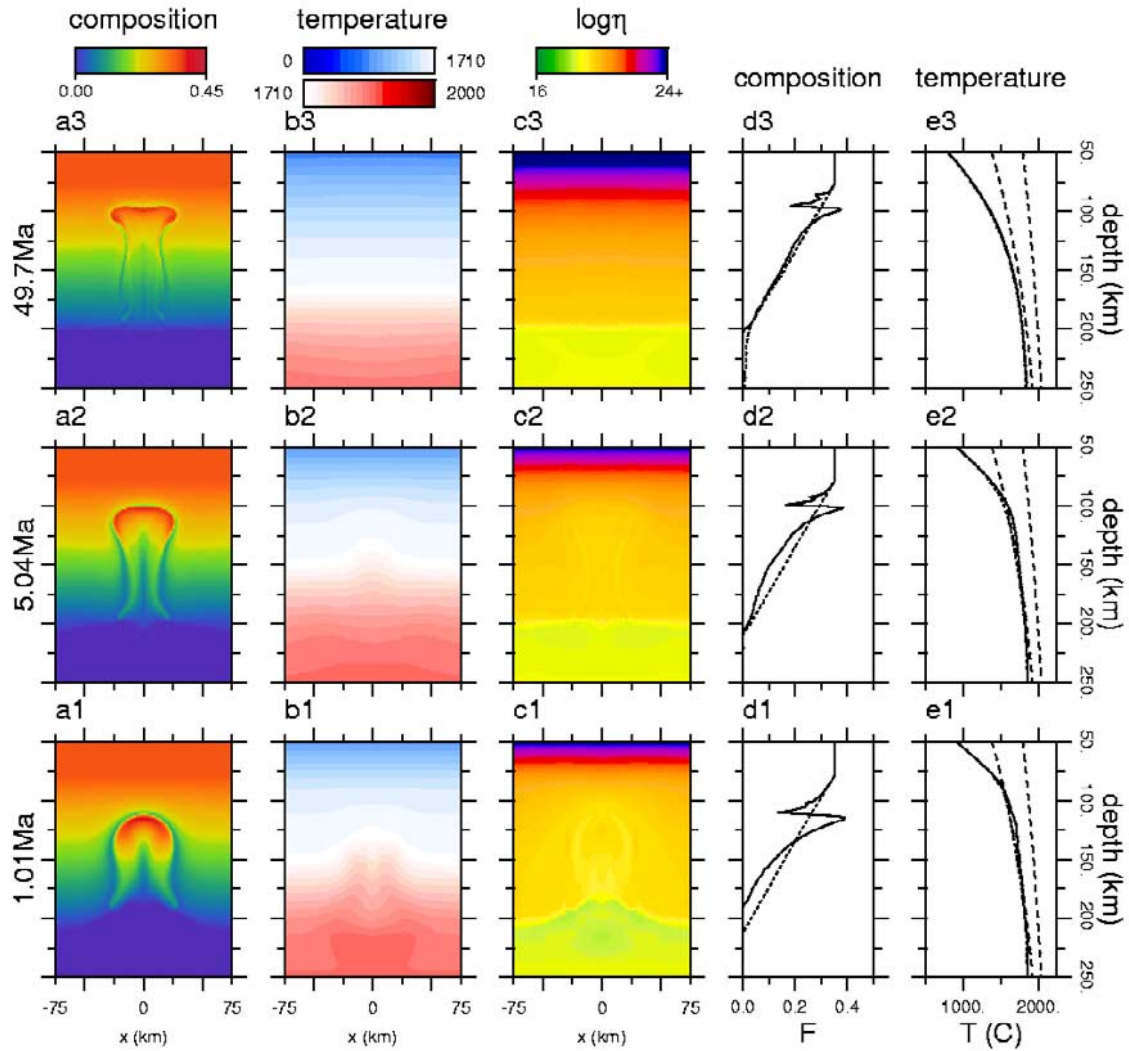


Figure 10. Model D1: Composite rheology, $f_{\eta} = 10$. Only a part of the domain is shown ($[x, y] = [-75-75, 50-250]$ km). Frames a1–3 show the composition field and frames b1–3 show the temperature field at 1.01 Myr, 5.04 Myr and 49.7 Myr after the start of the model run. Snapshots of the viscosity field are presented in frames c1–3. Profiles of composition and temperature are presented in frames d1–3 and e1–3, respectively. For an explanation of line types, see caption of Figure 2.

field, in which the effect is clearly recognizable in the viscosity contrast around 200 km depth which coincides with the bottom of the (chemical) root. The development of the diapir is illustrated in frames a1–3, which show the degree of depletion. The diapir develops a mushroom shape during its ascent to about 90 km depth, where the head flattens. The diapir reaches a minimum depth in about 10 Myr. The maximum degree of depletion attained is 0.39, as shown in frames d1–3.

[40] The dehydration prefactor in the viscosity model is increased to 50 in model D2, of which results are presented in Figure 11, and in Animation 2. Again the effect of the viscosity prefactor is clearly visible in the viscosity snapshots (frames c1–3). The diapir now rises more slowly (compared to model D1). It develops a similar mushroom shape, though it takes more time. The diapir head rises to about 100 km depth, which is reached in about 25 Myr. The maximum degree of depletion $F_{max} = 0.39$ is similar to that of model D1.

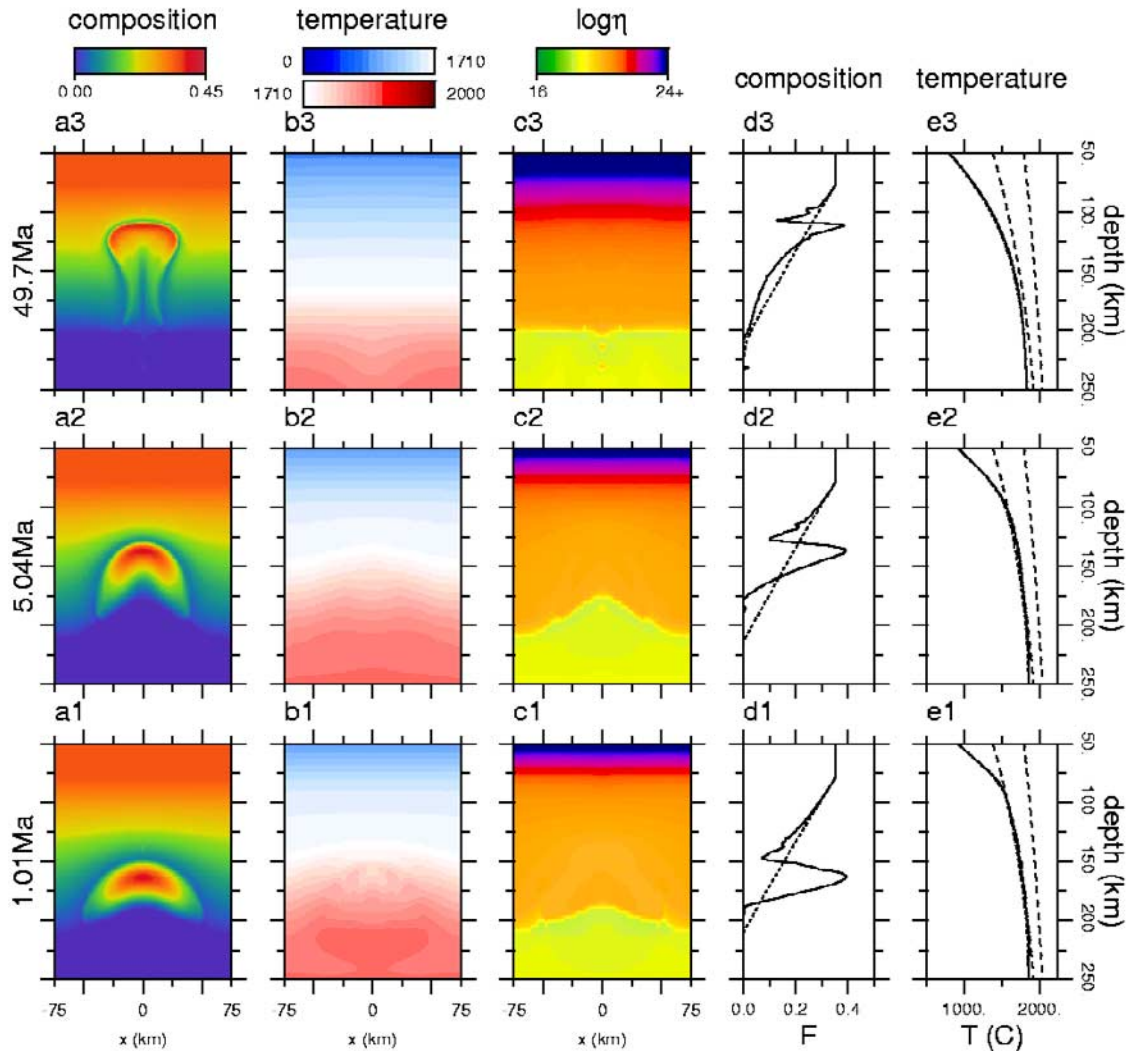


Figure 11. Model D2: Composite rheology, $f_{\eta} = 50$. Only a part of the domain is shown ($[x, y] = [-75-75, 50-250]$ km). Frames a1–3 show the composition field and frames b1–3 show the temperature field at 1.01 Myr, 5.04 Myr and 49.7 Myr after the start of the model run. Snapshots of the viscosity field are presented in frames c1–3. Profiles of composition and temperature are presented in frames d1–3 and e1–3, respectively. For an explanation of line types, see caption of Figure 2.

[41] Figure 12 shows results of model D3, which has a dehydration prefactor of 200 in the viscosity equation, slightly higher than the upper limit of 180 given by *Hirth and Kohlstedt* [1996]. This results in a strong viscosity contrast at the base of the lithospheric root at 200 km depth (see frames c1–3), where now also the shape of the melting diapir can be recognized in the viscosity fields, and a very slow penetration of the diapir into the root. The diapir head flattens during its ascent and has reached a depth of about 125 km at 49.7 Myr

(frame a3), where the ascent velocity is less than 1 mm/yr and still dropping.

3.7. Ascent Velocities

[42] Time series of the vertical velocity were calculated for a number of monitor tracer particles to determine the ascent velocity of the diapiric head. Representative results are presented in Figure 13. Two stages can be discerned for each model. During the initial stage, the diapir rises at

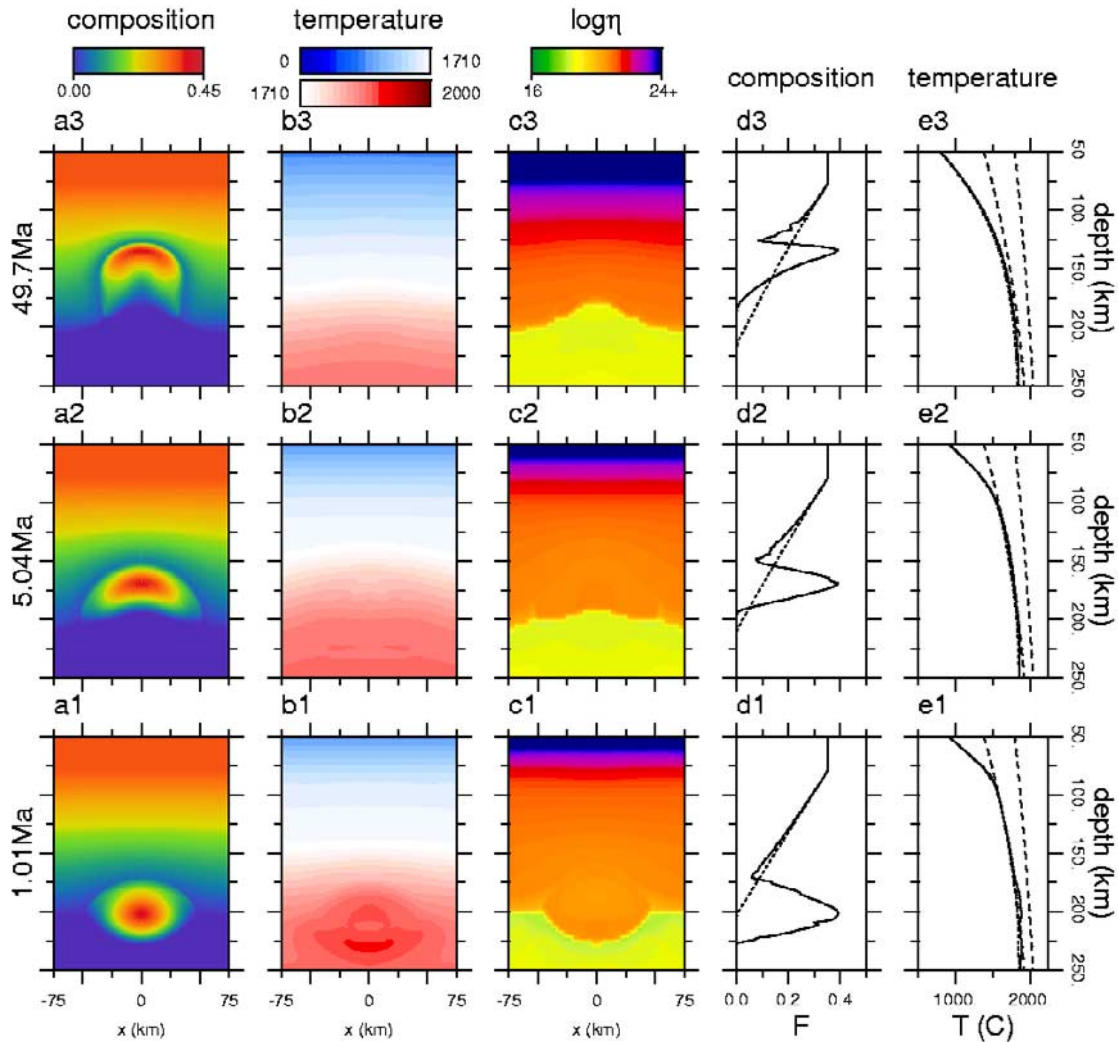


Figure 12. Model D3: Composite rheology, $f_{\eta} = 200$. Only a part of the domain is shown ($[x, y] = [-75-75, 50-250]$ km). Frames a1–3 show the composition field and frames b1–3 show the temperature field at 1.01 Myr, 5.04 Myr and 49.7 Myr after the start of the model run. Snapshots of the viscosity field are presented in frames c1–3. Profiles of composition and temperature are presented in frames d1–3 and e1–3, respectively. For an explanation of line types, see caption of Figure 2.

a more or less constant velocity. At some point the diapir starts to slow down as it encounters stiffer resistance.

[43] Model N1 (frame a) shows an ascent velocity which is several centimeters per year for about the first 10 million years, with a maximum of just over 10 cm/yr in the initial phase. Model N2, which has a somewhat weaker rheology, shows rapid ascent in the order of meters per year in the initial phase, but the velocity drops below 1 m/yr around 180 ka.

[44] The composite rheology models C1, C2 and C3 show similar shapes of the velocity evolution (Figure 13b), however with much higher velocities compared to model cases N1 and N2, with a high maximum value in the initial stage of nearly 1500 m/yr and values of several 100 m/yr during the first 500 years of the run. The velocity drops to about 100 m/yr at 1 ka and 1 cm/yr at 150 ka. Note that three almost identical curves are shown in Figure 13b, illustrating the self-regulating effect of the composite rheology, resulting in very similar ascent velocities for very different overall viscosities.

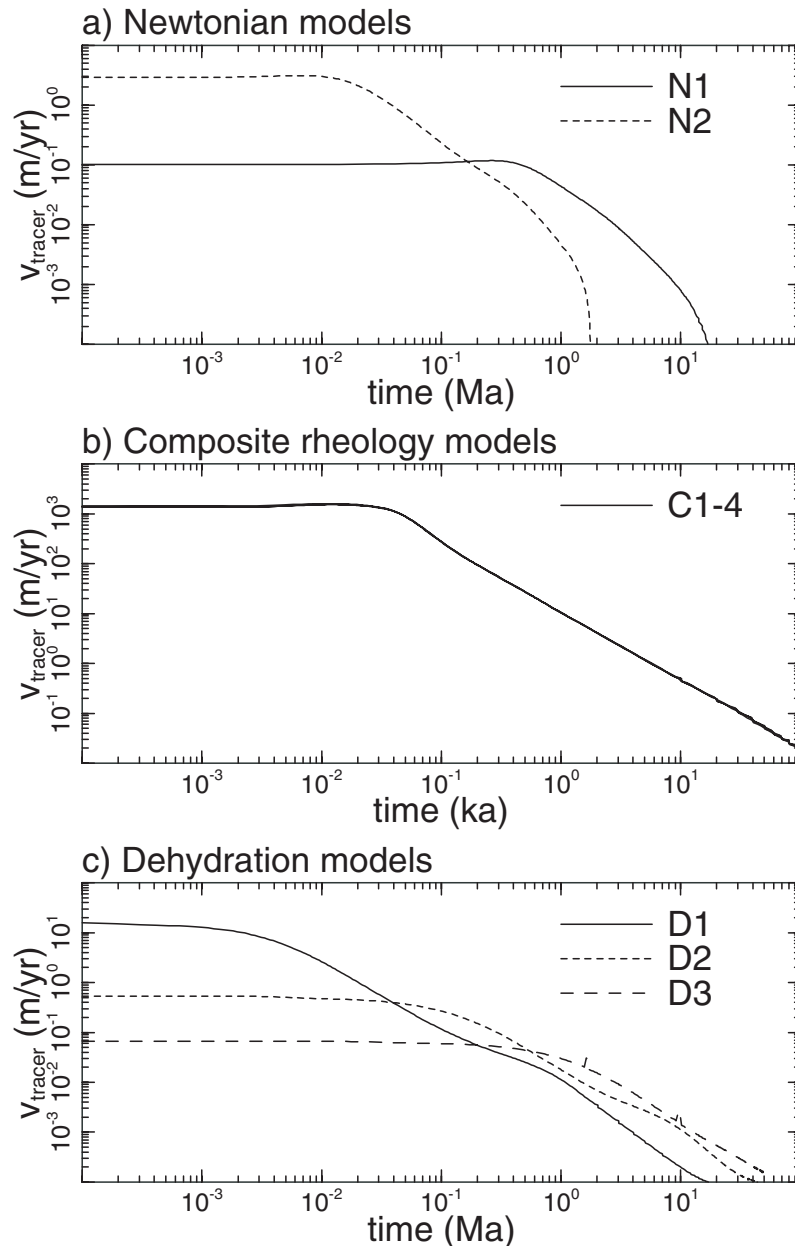


Figure 13. Time series of the vertical velocity of selected monitor tracers. Note the different time and velocity scales used in Figures 13a, 13b and 13c.

[45] The maximum vertical velocity for the dehydration models D1, D2 and D3 is 16 m/yr, 50 cm/yr and 8 cm/yr, respectively, attained in the early stages of diapir ascent (Figure 13c). The influence of the dehydration prefactor in the viscosity equation is evident from the lower ascent velocities compared to the composite rheology models. Compared to the composite rheology model C1, initial ascent velocities are 2 to 4 orders of magnitude lower. Velocities drop off to approximately 1 cm/yr

at 1.2 Myr, 1.6 Myr and 2.7 Myr, respectively, and continue to drop to negligible levels.

[46] We have tested the sensitivity of the model to the amplitude of the thermal perturbation which initiates the diapirs. Figure 14 shows three series of 3 snapshots of the degree of depletion field of a composite rheology model with grain size 1 mm and with three different perturbation amplitudes ϵ_T of 3%, 4% and 5%, respectively, of the background

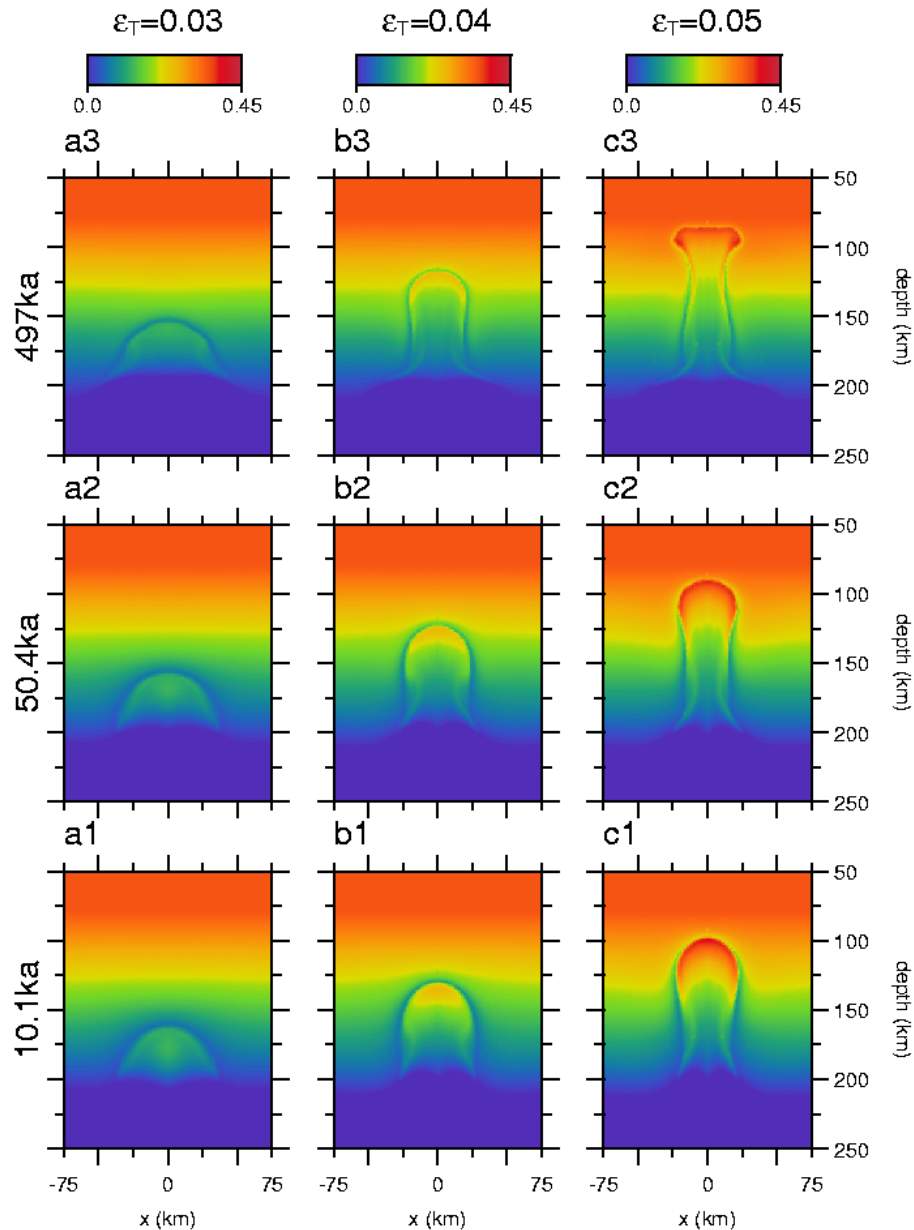


Figure 14. Diapir development for different values $\epsilon_T = \delta T/T(z)$ of the amplitude of the thermal perturbation which initiates the diapir. Values are fractions of the background temperature, which is about 1850 centigrade at the location of the initial perturbation. The other model parameters are the same as in case C2 (represented in the third column, see also Figure 5). The colour contours indicate the degree of depletion F .

temperature, which is approximately 1850 centigrade. The frames show the results to be quite sensitive to the amplitude of the initial perturbation.

[47] The maximum root mean square velocity V_{rms} [see *van den Berg et al.*, 1993] values observed have been plotted as a function of the relative amplitude ϵ_T of the thermal perturbation in Figure 15. The

maximum V_{rms} which was observed during a model run (generally during the initial phase of diapir ascent, illustrated in Figure 13) has been included in frame a, for three different model cases (composite 1mm(model case C2), dehydration 1mm with $f_\eta = 50$ (model case D2), and Newtonian 1mm (model case N2)). The curves in Figure 15a are shaped as the bottom end of a sigmoidal curve

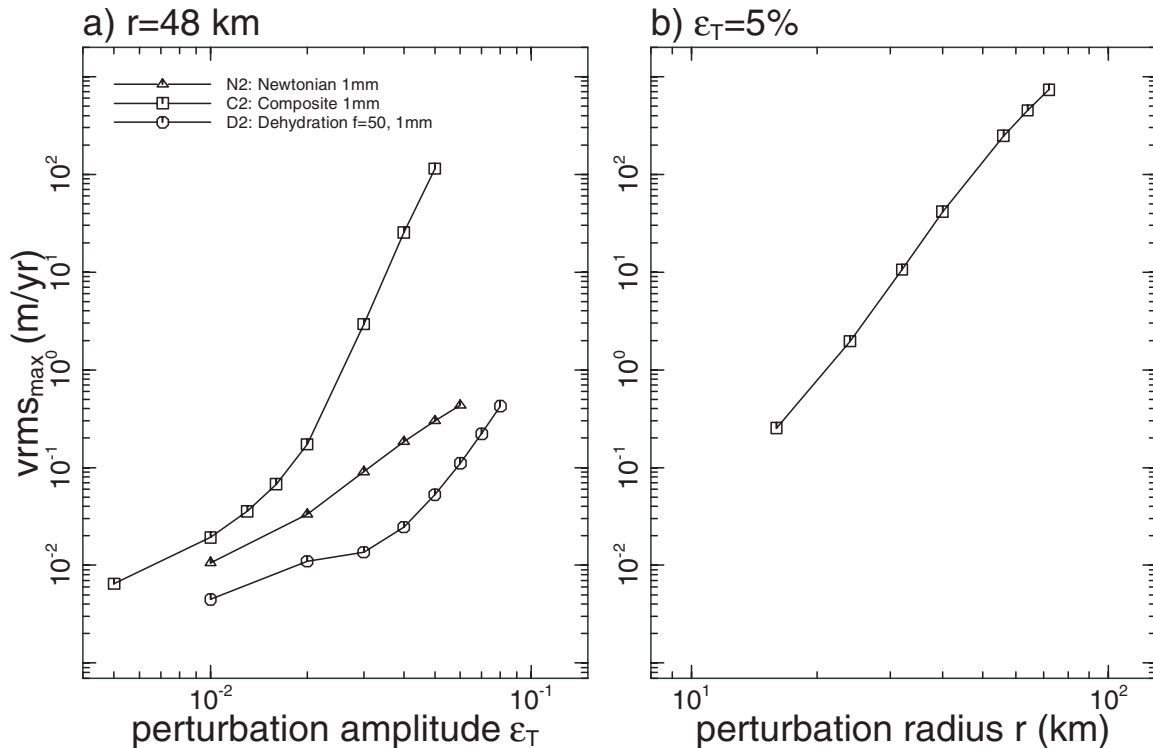


Figure 15. Variation of diapir ascent (measured as the maximum root mean square velocity of the domain) as a function of: (a) the perturbation amplitude $\epsilon_T = \delta T/T(z)$ at a constant 2σ (2 standard deviations) radius of 48 km; (b) the radius of the initial perturbation (2σ) at a constant ϵ_T of 5%.

(although the shape is less pronounced in the Newtonian case) revealing a transition between two different regimes. The lower amplitude part with a small slope represents cases where the diapir does not fully penetrate the continental root. The upper part with a larger slope corresponds to cases where the initial perturbation is greater than the critical value resulting in penetrating diapirs. Clearly, the transition between these regimes shifts to higher amplitudes ϵ_T considering successively stronger rheologies from composite C2, to Newtonian N2 to hydration dependent composite D2.

[48] Figure 15b shows the relation between the 2σ (2 standard deviations) radius of the thermal perturbation at a constant perturbation amplitude ϵ_T of 5% of the background temperature. The linear relation in log-log space is quite clear.

3.8. P,T Paths

[49] P,T paths of selected monitor tracers have been plotted in Figure 16, where separate tracers are indicated by different colours. Tracers were selected

on the basis of penetration to shallow depths and to show the variation of different paths to shallower levels. A P,T path inferred from cratonic peridotites [Drury *et al.*, 2001] has been included as a solid black line. Only one composite model is shown (C2), as the paths for the same tracers are quite similar in the other composite models. Although the timescales of the diapiric processes are vastly different for the different models, the resulting P,T paths are roughly the same for the cases shown, and similar to the inferred cratonic peridotite path by Drury *et al.* [2001] and model results by de Smet *et al.* [2000b] and Drury *et al.* [2001]. Such a similarity between paths derived from numerical models for diapirism and paths inferred for natural cratonic peridotites was also noted by Drury *et al.* [2001]. Some models show more cooling to lower temperatures (N2, D1) than other models (C2) but this is mainly caused by the running time of the different models, ranging from 497 ka for the composite models to 49.7 Myr for the Newtonian and dehydration models. The short length of the cooling leg (almost horizontal line) of the paths in

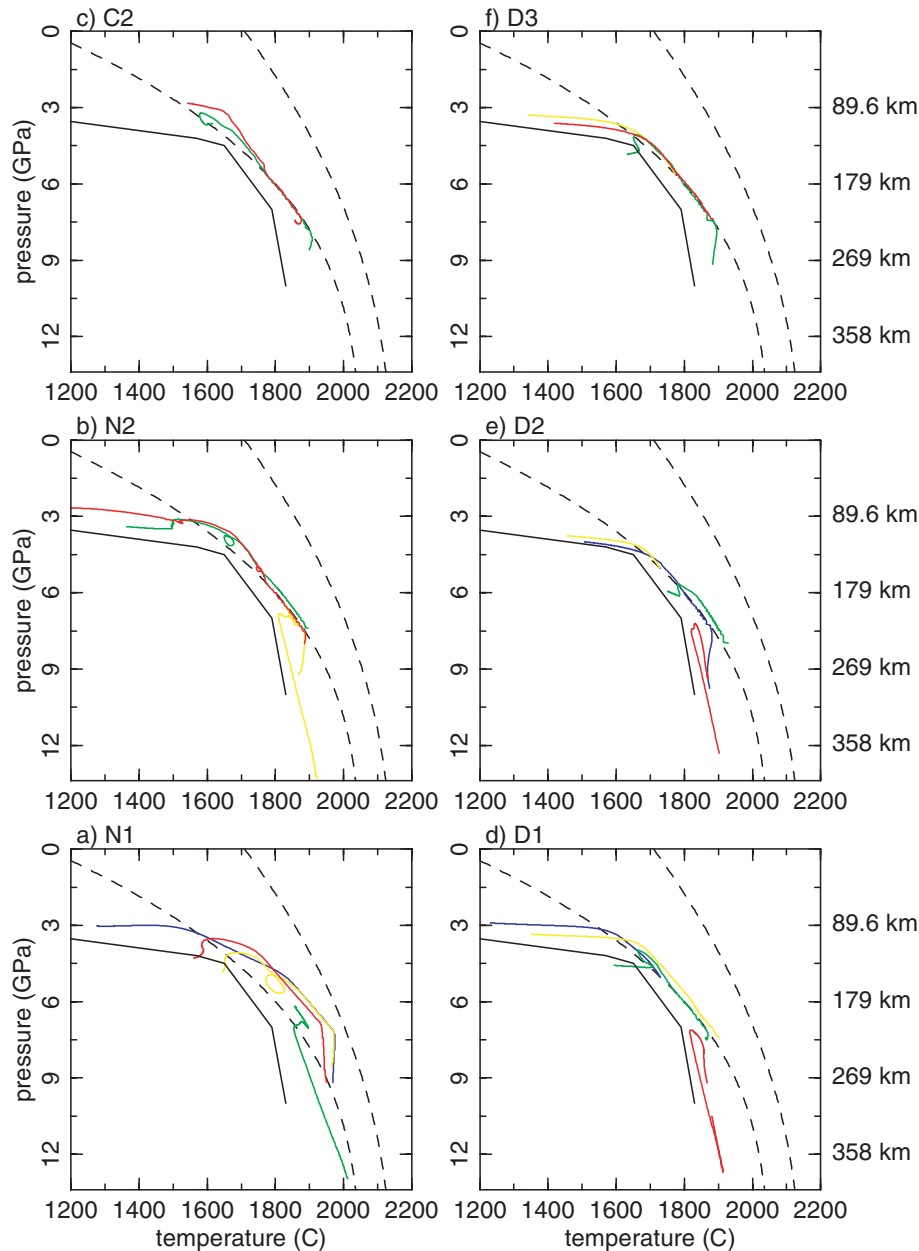


Figure 16. Pressure-temperature paths for selected monitor tracers, each indicated by a different colour. The solidus and liquidus (third-order parameterization) are indicated by dashed lines. Also included (in a black solid line) are inferred P,T paths from eclogites of the Western Gneiss Region, Norway [Drury *et al.*, 2001]. (a) Model N1, running time is 49.7 Myr, (b) model N2, running time is 49.7 Myr, (c) model C2 (models C1, C3 and C4 are similar), running time 497 ka, (d) model D1, running time 49.7 Myr, (e) model D2, running time 49.7 Myr, (f) model D3, running time 49.7 Myr.

models D2 and D3 is caused by the low ascent velocity of these models, such that conductive cooling becomes important only at a late stage.

3.9. Stress and Strain Rate Histories

[50] Grain size characteristics of rock samples can render estimates of the stress and strain rate history

of these rocks, and may therefore be a link between our numerical modeling results and the real Earth. We have used monitor tracer particles to log the second invariant of the local strain rate and stress tensors in time. The modeling results reveal that the maximum strain rates and stresses observed depend quite strongly on the viscosity model. Only monitor particles are presented which experienced partial

Table 5. Maximum Observed Values for the Second Invariant of the Strain Rate Tensor and the Second Invariant of the Stress Tensor, Respectively^a

Model	Maximum Strain Rate, s^{-1}	Maximum Stress, Pa
N1	7.53×10^{-14}	1.21×10^6
N2	1.62×10^{-12}	4.90×10^6
C1	1.28×10^{-9}	3.68×10^6
C2	1.25×10^{-9}	3.66×10^6
C3	1.25×10^{-9}	3.66×10^6
C4	1.25×10^{-9}	3.66×10^6
D1	1.75×10^{-11}	5.43×10^6
D2	5.93×10^{-13}	7.27×10^6
D3	3.16×10^{-13}	7.97×10^6

^aOnly monitor tracers that have undergone partial melting during the model run have been considered.

melting, and which were part of the diapir. Maximum strain rate and stress values which were observed are presented in Table 5, and the stress and strain rate versus depth for selected tracer particles are plotted in Figure 17. The maximum stresses observed which are listed in Table 5 vary by less than one order of magnitude. The maximum strain rates, however, vary over nearly five orders of magnitude. The Newtonian models N1 and N2 have maximum strain rates of $7.53 \times 10^{-14} s^{-1}$ and $1.62 \times 10^{-12} s^{-1}$, respectively. This difference is caused by the smaller grain size and therefore lower viscosity of the latter model. The four composite rheology models C1–4 show very similar maximum strain rate values, much higher (3–5 orders of magnitude) than those observed for the Newtonian models, just over $1 \times 10^{-9} s^{-1}$. Here, the effect of the nonlinear component of the rheology becomes apparent. As can be expected, the dehydration models show lower strain rates because of their higher viscosities, ranging from $1.75 \times 10^{-11} s^{-1}$ to $3.16 \times 10^{-13} s^{-1}$ for models D1 to D3.

4. Discussion and Conclusions

[51] Comparison of the results of models N1 and N2 versus models C1–4 show that the addition of a nonlinear creep component to the Newtonian diffusion creep component of the rheology model strongly increases the ascent velocity and thus reduces the characteristic emplacement timescale for a diapir considerably to less than a conservative hundred thousand years. The results of model C5

(relative to model C1) show that a third-order parameterization of solidus and liquidus, based on *Herzberg and Zhang* [1996] (used in models N2, C1–4 and D1–3), strongly favors diapir development relative to a linear parameterization. The latter third-order parameterization allows for melting at lower temperatures for depths greater than about 200 km than the former linear, thus facilitating melting at these depths. Depletion-induced compositional buoyancy further drives the upward movement of the diapir, thus providing a self-accelerating mechanism for diapir intrusion into and within a continental root. This illustrates the importance of compositional differentiation in the evolution of mantle diapirs.

[52] The results of all models show locally sharp variations in the degree of depletion, most readily observable in the degree of depletion profiles (frames d1–3) of the model result Figures 2–7 and 10–12. Numerical models have indicated that these sharp compositional variations in the lithosphere resulting from mantle diapirism of the kind investigated here may act as seismic P-wave reflectors [*de Smet et al.*, 1999]. Possibly, the sheetlike structures of flattened diapir heads, as predicted by some of our models for a composite rheology, will be detectable in the uppermost mantle by seismic methods as have been applied in recent mantle reflection seismic studies [e.g., *Pavlenkova and Yegorkin*, 1983; *Ellis et al.*, 1996; *Pavlenkova et al.*, 1996].

[53] Another aspect related to direct observables is the seismic anisotropy which may be created by the deformation processes included in our models [see, e.g., *Tommasi et al.*, 1999]. *Silver et al.* [2001] find evidence for preservation of Archean mantle deformation in small or vertically incoherent seismic anisotropy in their region of study (Kaapvaal and Zimbabwe cratons).

[54] The results of the modeling experiments show that a relatively large variations in grain size (two orders of magnitude, which translates to five orders of magnitude in the diffusion creep viscosity prefactor through the grain size exponent $m = 2.5$) have a limited effect on the dynamics of the diapirs modeled in this work. Although the dominant

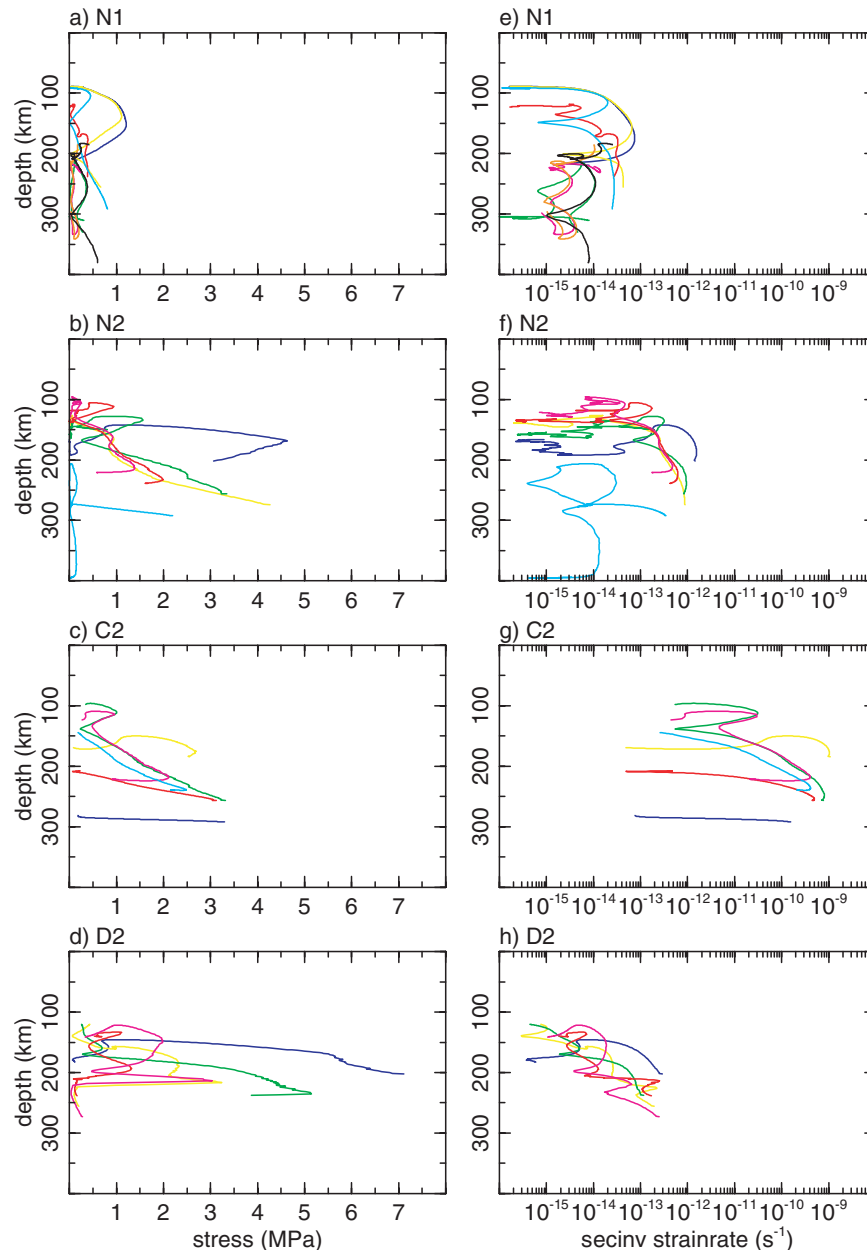


Figure 17. Paths for selected tracers of model(s) N1, N2, C2 and D2 in stress–depth space and strain rate–depth space, respectively. Figures 17a–17d show the stress as a function of depth for these models, and Figures 17e–17h show the second invariant of the strain rate as a function of depth for selected monitor particle tracers.

creep mechanism clearly shifts from diffusion creep to dislocation creep as a result of increasing the grain size parameter, the overall dynamics of the different cases are roughly similar. Detailed analysis of snapshots of the viscosity field reveals a localized zone of high stress and strain rate and low viscosity surrounding the diapiric head. Roughly the same viscosity minima are found in this localized deformation zone for the different composite

rheology cases, indicating that a self-regulating mechanism is operative, controlling the ascent.

[55] Concerning the effect of dehydration on the rheology, we have found that this has a strong effect on diapir dynamics. Although two of the three depletion viscosity factors are smaller than those reported by *Hirth and Kohlstedt* [1996] (factor 100–180), it is quite apparent from the

results of models D1, D2 and D3 (Figures 10, 11 and 12) that even the effect of a relatively small dehydration factor (as low as 10) is considerable. This smaller factor may be justified by assuming that the material becomes (partially) rehydrated by mobile volatile phases originating from other areas of partial melting, since studies of craton xenoliths show evidence for rehydration [Harte, 1983]. The fact that peridotites have been emplaced in the Archean at depths of up to 100 km [Drury *et al.*, 2001], and that this depth is not reached by the diapir model with maximum dehydration prefactor $f_{\eta} = 200$ (model D3, Figure 12) suggests that during the Archean the rheology of the cratonic lithosphere was not completely dry. The model case C2 is used as a reference (Figure 5) in the investigation of the effect of the viscosity factor f_{η} . The shape of the diapir head, the vertical velocity of the diapir and the level to which the diapir penetrates are all strongly influenced by this dehydration factor. With increasing viscosity factor, the shape tends to be more mushroom-like, the ascent velocity of the diapir decreases and the penetrating power is diminished as well.

[56] The different experiments which we have conducted have yielded diapirs showing ascent velocities of several centimeters per year for purely Newtonian model N1 and dehydration model D3 (factor 200) up to several hundred meters per year for the composite rheology models C1, C2, C3 and C4. Although these high end values seem extreme, other workers have reported high velocities in non-Newtonian mantle models. Larsen *et al.* [1997] and Larsen and Yuen [1997] report ascent velocities for non-Newtonian diapirs over 10 m/yr. Weinberg and Podladchikov [1994] showed that a diapir may rise with velocities of 10–100 m/yr into the middle or upper crust if the wall rock exhibits power law behavior, and Solomatov and Moresi [2000] find velocities of several meters per year for cold plumes formed in a stagnant lid regime convection model. The very high ascent velocities in our models are also facilitated by weakening of the surrounding rock by a large strain rate and a power law rheology (the dislocation creep component), as can be observed in frames c1–3 of Figures 4–7.

[57] A comparison of stress and strain rate histories obtained in this study with geological observations might help to constrain models of mantle diapirism in view of the large uncertainty in the model parameters applied. Structures and microstructures in these mantle rocks provide some independent control on the conditions of deformation during diapir upwelling in cratonic lithosphere. The differential stress during high temperature deformation can be estimated from the dynamic recrystallized grain size. If the temperature during deformation is known then strain rates can be estimated from the stress and temperature estimates.

[58] The stress and strain rate histories within the model diapirs show relatively high initial strain rates (up to 10^{-10} to 10^{-9} s⁻¹ for model C2, see Figure 17 and Table 5) and stress levels (2–7 MPa). The dynamic recrystallized grain size produced during the initial diapir intrusion should be around 1 to 15 mm. As upwelling continues stress and strain rate decrease overall, although many tracers experience a strain rate and stress pulse at shallow depths with stress levels up to 1 MPa. The last stages of deformation at shallow depth occur with decreasing stress and strain rate at stress levels less than 1 to 0.5 MPa. The decaying strain rates can be related to the cooling of the diapir as it accretes into the lithosphere. If the dynamic recrystallized grain size remained “in equilibrium” with the stress in the final stages of deformation then a grain size between 1.5–10 cm would be expected. This estimate of the dynamically recrystallized grain size is based on an experimental calibration for olivine with low water content over a temperature range of 1100–1650C [Karato *et al.*, 1980; van der Wal *et al.*, 1993]. As the diapir cools down the stress and strain rate decrease to very low values such that the material will become “annealed.” In this situation the grain size will be modified by static recrystallization with the grain size depending on the amount of residual strain in the grains, the time of annealing and the temperature during annealing.

[59] In the cratonic peridotites from Norway and kimberlite xenoliths the average grain sizes are in the range of 0.5 to 10 mm [Avé Lallemant *et al.*, 1980; van Roermund *et al.*, 2001]. The micro-

structures of the Norwegian peridotites are consistent with significant static recrystallization as strain free grains (1–4 mm) have replaced much larger deformed grains (1–10 cm diameter). Similar trends are found in kimberlite xenoliths and in the spinel peridotites from the North Pyrenean fault zone [Fabriès *et al.*, 1991]. The large grain sizes found as relict grains in the cratonic peridotites are consistent with the grain size to be expected from the numerical models. The large grain sizes (1–30 cm) found as relict grains in the cratonic peridotites are consistent with the dynamic recrystallized grain size predicted (1.5–10 cm) from the stress levels in the numerical models for the last stage of deformation. The static recrystallized microstructure of cratonic peridotites is also consistent with the thermomechanical history of diapirs in the numerical models. In the Norwegian peridotites, however, the recrystallized grain size is smaller than the initial grain size which suggests a more complex history with a second deformation and recrystallization cycle, possibly related to later subduction and exhumation, supercilious on the coarse microstructure produced by diapiric intrusion.

[60] Rough estimates of the strain rates during the high temperature history of the Norwegian cratonic peridotites can be made from stress and temperature estimates combined with experimental flow laws. For a stress of 0.5 MPa and a temperature range of 1350–1600°C estimated from early mineral assemblages [van Roermund and Drury, 1998; Drury *et al.*, 2001] strain rates in the range of 7×10^{-15} to $1.4 \times 10^{-12} \text{ s}^{-1}$ are indicated for dry olivine and 1.4×10^{-12} to $2.0 \times 10^{-10} \text{ s}^{-1}$ for wet olivine [Chopra and Paterson, 1984]. This broad range of strain rates is compatible with strain rates obtained from the numerical models (Figure 17) during the last stages of diapir intrusion into the lithosphere.

[61] Note that local strain rates in the diapir can be very high and much higher than strain rates expected from typical plate tectonic rates. Some spectacularly sheared xenoliths are found in kimberlites [Nixon and Boyd, 1973; Boullier and Nicolas, 1973] and estimates of deformation conditions imply very high stress and strain rates [Goezte, 1978; Mercier, 1979]. Kimberlite magma-

tism may be associated with diapirs in the modern mantle [Green and Gueguen, 1983; Haggerty, 1994]. These diapirs would be quite different from those modeled in this study, if only because the potential temperature of the mantle is of the order of 300 centigrade lower, which strongly increases viscosities. However, we note that the very high strain rates and stress levels estimated for the sheared xenoliths could be consistent with deformation during diapiric intrusion, although this would need to be tested with models which include wet melting in a modern mantle.

Acknowledgments

[62] We thank Michel Jacobs for helpful discussions concerning thermodynamic aspects of the work and David Yuen and Alison Leitch for their constructive reviews of the manuscript.

References

- Arndt, N., C. Ginibre, C. Chauvel, F. Albarède, M. Cheadle, C. Herzberg, G. Jenner, and Y. Lahay, Were komatiites wet?, *Geology*, *26*, 739–742, 1998.
- Avé Lallemant, H. G., N. L. Carter, J.-C. C. Mercier, and J. V. Ross, Rheology of the uppermost mantle: Inferences from peridotite xenoliths, *Tectonophysics*, *70*, 1–27, 1980.
- Boullier, A.-M., and A. Nicolas, Texture and fabric of peridotite nodules from kimberlite at Mothae, Thaba Putsoa and Kimberley, in *Lesotho Kimberlites*, pp. 57–66, Lesotho Natl. Dev. Corp., Meseru, Lesotho, 1973.
- Braun, J., J. Chery, A. Poliakov, D. Mainprice, A. Vauchez, A. Tomassi, and M. Daignieres, A simple parameterization of strain localization in the ductile regime due to grain size reduction: A case study for olivine, *J. Geophys. Res.*, *104*, 25,167–25,181, 1999.
- Bruceknier, H. K., and L. G. Medaris, A tale of two orogens: The contrasting T-P-t history and geochemical evolution of mantle in high and ultra-high pressure metamorphic terranes of the Norwegian Caledonides and the Czech Variscides, *Schweiz. Mineral. Petrogr. Mitt.*, *78*, 293–307, 1998.
- Buck, W. R., and W. Su, Focused mantle upwelling below mid-ocean ridges due to feedback between viscosity and melting, *Geophys. Res. Lett.*, *16*(7), 641–644, 1989.
- Campbell, I. H., and R. I. Hill, A two-stage model for the formation of the granite-greenstone terrains of the Kalgoorlie-Norseman area, Western Australia, *Earth Planet. Sci. Lett.*, *90*, 11–25, 1988.
- Chopra, P. N., and M. S. Paterson, The experimental deformation of dunite, *Tectonophysics*, *78*, 453–473, 1981.
- Chopra, P., and M. S. Paterson, The role of water in the deformation of dunite, *J. Geophys. Res.*, *89*, 7861–7876, 1984.
- de Bresser, J. H. P., C. J. Peach, J. P. J. Reijs, and C. J. Spiers, On dynamic recrystallization during solid state flow: Effects

- of stress and temperature, *Geophys. Res. Lett.*, *25*(18), 3457–3460, 1998.
- de Bresser, J. H. P., J. H. ter Heege, and C. J. Spiers, Grain size reduction by dynamic recrystallization: Can it result in major rheological weakening?, *Int. J. Earth Sci.*, *90*(1), 28–45, 2001.
- de Smet, J. H., The evolution of the continental upper mantle: Numerical modelling of thermo-chemical convection including partial melting, Ph.D. thesis, University of Utrecht, Utrecht, Netherlands, 1999.
- de Smet, J. H., A. P. van den Berg, and N. J. Vlaar, Stability and growth of continental shields in mantle convection models including recurrent melt production, *Tectonophysics*, *296*, 15–29, 1998.
- de Smet, J. H., A. P. van den Berg, and N. J. Vlaar, The evolution of continental roots in numerical thermo-chemical mantle convection models including differentiation by partial melting, *Lithos*, *48*, 153–170, 1999.
- de Smet, J. H., A. P. van den Berg, N. J. Vlaar, and D. A. Yuen, A characteristics-based method for solving the transport equation and its application to the process of mantle differentiation and continental root growth, *Geophys. J. Int.*, *140*, 651–659, 2000a.
- de Smet, J. H., A. P. van den Berg, and N. J. Vlaar, Early formation and long-term stability of continents resulting from decompression melting in a convecting mantle, *Tectonophysics*, *322*, 19–33, 2000b.
- Drury, M. R., and J. D. Fitz Gerald, Mantle rheology: Insights from laboratory experiments on mineral deformation and transformation, in *The Earth's Mantle*, pp. 503–559, Cambridge Univ. Press, New York, 1998.
- Drury, M. R., H. L. M. van Roermund, D. A. Carswell, J. H. de Smet, A. P. van den Berg, and N. J. Vlaar, Emplacement of deep upper mantle rocks into cratonic lithosphere by convection and diapiric upwelling, *J. Petrol.*, *42*, 131–140, 2001.
- Ellis, R. M., Z. Hajnal, and M. G. Bostock, Seismic studies on the trans-Hudson orogen of Western Canada, *Tectonophysics*, *262*, 35–50, 1996.
- Fabriès, J., J. P. Lorand, J. L. Bodinier, and C. Dupuy, Evolution of the upper mantle beneath the Pyrenees: Evidence from orogenic spinel lherzolite massifs, *J. Petrol.*, *32*, 55–76, 1991.
- Fei, Y., H. Mao, and B. O. Mysen, Experimental determination of element partitioning and calculation of phase relations in the MgO-FeO-SiO₂ system at high pressure and high temperature, *J. Geophys. Res.*, *96*, 2157–2169, 1991.
- Goetze, C., Sheared lherzolites from the point of view of rock mechanics, *Geology*, *3*, 172–173, 1978.
- Green, H. W., and Y. Gueguen, Deformation of peridotite in the mantle and extraction by kimberlite: A case history documented by fluid and solid precipitates in olivine, *Tectonophysics*, *92*, 71–92, 1983.
- Haggerty, S. E., Superkimberlites: A geodynamic diamond window to the Earth's core, *Earth Planet. Sci. Lett.*, *122*, 57–69, 1994.
- Harte, B., Mantle peridotites and processes: The kimberlite sample, in *Continental Basalts and Mantle Xenoliths*, edited by C. J. Hawkesworth and M. J. Norry, pp. 46–91, Birkhäuser Boston, Cambridge, Mass., 1983.
- Herzberg, C., and M. J. O'Hara, Phase equilibrium constraints on the origin of basalts, picrites and komatiites, *Earth Sci. Rev.*, *44*(1–2), 39–79, 1998.
- Herzberg, C., and J. Zhang, Melting experiments on anhydrous peridotite KLB-1: Compositions of magmas in the upper mantle and the transition zone, *J. Geophys. Res.*, *101*, 8271–8295, 1996.
- Hirth, G., and D. L. Kohlstedt, Water in the oceanic upper mantle: Implications for rheology, melt extraction and the evolution of the lithosphere, *Earth Planet. Sci. Lett.*, *144*, 93–108, 1996.
- Hockney, R. W., and J. W. Eastwood, *Computer Simulation Using Particles*, Inst. of Phys., Philadelphia, Pa., 1988.
- Ito, G., Reykjanes 'V' shaped ridges originating from a pulsing and dehydrating mantle plume, *Nature*, *411*, 681–684, 2001.
- Ito, G., Y. Shen, G. Hirth, and C. J. Wolfe, Mantle flow, melting, and dehydration of the Iceland mantle plume, *Earth Planet. Sci. Lett.*, *165*, 81–96, 1999.
- Jaques, A. L., and D. H. Green, Anhydrous melting of peridotite at 0–15 Kb pressure and the genesis of tholeiitic basalts, *Contrib. Mineral. Petrol.*, *73*, 287–310, 1980.
- Jha, K., E. M. Parmentier, and J. P. Morgan, The role of mantle-depletion and melt-retention buoyancy in spreading-center segmentation, *Earth Planet. Sci. Lett.*, *125*, 221–234, 1994.
- Jordan, T. H., Mineralogies, densities, and seismic velocities of garnet lherzolites and their geophysical implications, in *The Mantle Sample: Inclusions in Kimberlites and Other Volcanics*, pp. 1–14, AGU, Washington, D.C., 1979.
- Jung, H., and S.-I. Karato, Effects of water on dynamically recrystallized grain-size of olivine, *J. Struct. Geol.*, *23*, 1337–1344, 2001.
- Kameyama, M., D. A. Yuen, and H. Fujimoto, The interaction of viscous heating with grain-size dependent rheology in the deformation of localized slip zones, *Geophys. Res. Lett.*, *24*(20), 2523–2526, 1997.
- Karato, S., Does partial melting reduce the creep strength of the upper mantle?, *Nature*, *319*, 309–310, 1986.
- Karato, S.-I., and H. Jung, Water, partial melting and the origin of the seismic low velocity and high attenuation zone in the upper mantle, *Earth Planet. Sci. Lett.*, *157*, 193–207, 1998.
- Karato, S.-I., and P. Wu, Rheology of the upper mantle: A synthesis, *Science*, *260*, 771–778, 1993.
- Karato, S.-I., M. Toriumi, and T. Fujii, Dynamic recrystallization of olivine single crystals during high-temperature creep, *Geophys. Res. Lett.*, *7*(9), 649–652, 1980.
- Karato, S., S. Q. Zhang, and H. R. Wenk, Superplasticity in the Earth's lower mantle: Evidence from seismic anisotropy and rock physics, *Science*, *270*, 458–461, 1995.
- Lambeck, K., C. Smither, and P. Johnston, Sea-level change, glacial rebound and mantle viscosity for northern Europe, *Geophys. J. Int.*, *134*, 102–144, 1998.
- Larsen, T. B., and D. A. Yuen, Ultrafast upwelling bursting through the upper mantle, *Earth Planet. Sci. Lett.*, *146*, 393–399, 1997.
- Larsen, T. B., D. A. Yuen, J. L. Smedsmo, and A. V. Malevsky, Generation of fast timescale phenomena in thermo-mechanical processes, *Phys. Earth Planet. Inter.*, *102*, 213–222, 1997.

- Larsen, T. B., D. A. Yuen, and M. Storey, Ultrafast mantle plumes and implications for flood basalt volcanism in the northern Atlantic region, *Tectonophysics*, 311, 31–43, 1999.
- McKenzie, D. P., and M. J. Bickle, The volume and composition of melt generated by extension of the lithosphere, *J. Petrol.*, 29(3), 625–679, 1988.
- Mei, S., and D. L. Kohlstedt, Influence of water on plastic deformation of olivine aggregates, 1, Diffusion creep regime, *J. Geophys. Res.*, 105, 21,457–21,469, 2000a.
- Mei, S., and D. L. Kohlstedt, Influence of water on plastic deformation of olivine aggregates, 2, Dislocation creep regime, *J. Geophys. Res.*, 105, 21,471–21,481, 2000b.
- Mercier, J.-C. C., Peridotite xenoliths and the dynamics of kimberlite intrusions, in *The Mantle Sample: Inclusions in Kimberlites and Other Volcanics*, edited by F. R. Boyd and H. O. Meyer, pp. 197–212, AGU, Washington, D. C., 1979.
- Nicolas, A., Structure and petrology of peridotites: Clues to their geodynamic environment, *Rev. Geophys.*, 24, 875–895, 1986.
- Nicolas, A., F. Lucazeau, and R. Bayer, Peridotite xenoliths in Massif Central basalts, France: Textural and geophysical evidence for asthenospheric diapirism, in *Mantle Xenoliths*, edited by P. H. Nixon, pp. 563–574, Wiley-Intersci., New York, 1987.
- Nisbet, E. G., M. J. Cheadle, N. T. Arndt, and M. J. Bickle, Constraining the potential temperature of the Archaean mantle: A review of the evidence from komatiites, *Lithos*, 30, 291–307, 1993.
- Nixon, P. H., and F. R. Boyd, Petrogenesis of the granular and sheared ultrabasic nodule suite in kimberlites, in *Lesotho Kimberlites*, edited by P. H. Nixon, pp. 48–56, Lesotho Natl. Dev. Corp., Maseru, Lesotho, 1973.
- Parman, S. W., J. C. Dann, T. L. Grove, and M. J. de Wit, Emplacement conditions of komatiite magmas from the 3.49 Ga Komati formation, Barberton Greenstone Belt, South Africa, *Earth Planet. Sci. Lett.*, 150, 303–323, 1997.
- Pavlenkova, N. I., and A. V. Yegorkin, Upper mantle heterogeneity in the northern part of Eurasia, *Phys. Earth Planet. Inter.*, 33, 180–193, 1983.
- Pavlenkova, N. I., G. A. Pavlenkova, and L. N. Solodilov, High velocities in the uppermost mantle of the Siberian Craton, *Tectonophysics*, 262, 51–65, 1996.
- Richter, F. M., Models for the Archean thermal regime, *Earth Planet. Sci. Lett.*, 73, 350–360, 1985.
- Ross, J. V., H. G. Ave Lallemand, and N. L. Carter, Stress dependence of recrystallized-grain and subgrain size in olivine, *Tectonophysics*, 70, 39–61, 1980.
- Rutter, E. H., and K. Brodie, The role of tectonic grain size reduction in the rheological stratification of the lithosphere, *Geol. Rundsch.*, 77(1), 295–308, 1988.
- Scott, D. R., and D. J. Stevenson, A self-consistent model of melting, magma migration and buoyancy-driven circulation beneath mid-ocean ridges, *J. Geophys. Res.*, 94, 2973–2988, 1989.
- Silver, P. G., S. S. Gao, and K. H. Liu, Mantle deformation beneath southern Africa, *Geophys. Res. Lett.*, 28(13), 2493–2496, 2001.
- Solomatov, V. S., and L.-N. Moresi, Scaling of time-dependent stagnant lid convection: Application to small-scale convection on Earth and other terrestrial planets, *J. Geophys. Res.*, 105, 21,795–21,817, 2000.
- Stone, W. E., E. Deloule, M. S. Larson, and C. M. Leshar, Evidence for hydrous high-MgO melts in the Precambrian, *Geology*, 25, 143–146, 1997.
- Takahashi, E., and I. Kushiro, Melting of dry peridotite at high pressures and basalt magma genesis, *Am. Mineral.*, 68, 859–879, 1983.
- Tommasi, A., B. Tikoff, and A. Vauchez, Upper mantle tectonics: Three-dimensional deformation, olivine crystallographic fabrics and seismic properties, *Earth Planet. Sci. Lett.*, 168, 173–186, 1999.
- van den Berg, A. P., and D. A. Yuen, Is the lower-mantle rheology Newtonian today?, *Geophys. Res. Lett.*, 23(16), 2033–2036, 1996.
- van den Berg, A. P., and D. A. Yuen, The role of shear heating in lubricating mantle flow, *Earth Planet. Sci. Lett.*, 151, 33–42, 1997.
- van den Berg, A. P., and D. A. Yuen, Modelling planetary dynamics by using the temperature at the core-mantle boundary as a control variable: Effects of rheological layering on mantle heat transport, *Phys. Earth Planetary Inter.*, 108, 219–234, 1998.
- van den Berg, A. P., P. E. van Keken, and D. A. Yuen, The effects of a composite non-Newtonian and Newtonian rheology on mantle convection, *Geophys. J. Int.*, 115, 62–78, 1993.
- van der Wal, D., P. Chopra, M. Drury, and J. Fitz Gerald, Relationships between dynamically recrystallized grain size and deformation conditions in experimentally deformed olivine rocks, *Geophys. Res. Lett.*, 20(14), 1479–1482, 1993.
- van Keken, P. E., Evolution of starting mantle plumes: A comparison between numerical and laboratory experiments, *Earth Planet. Sci. Lett.*, 148, 1–11, 1997.
- van Keken, P. E., S. D. King, H. Schmeling, U. R. Christensen, D. Neumeister, and M.-P. Doin, A comparison of methods for the modeling of thermochemical convection, *J. Geophys. Res.*, 102, 22,477–22,495, 1997.
- van Roermund, H. L. M., and M. R. Drury, Ultra-high pressure ($P > 6$ GPa) garnet peridotites in western Norway: Exhumation of mantle rocks from more than 185 km, *Terra Nova*, 10, 295–301, 1998.
- van Roermund, H. L. M., M. Drury, A. Barnhoorn, and A. de Ronde, Relict majoritic garnet microstructures from ultra-deep orogenic peridotites in western Norway, *J. Petrol.*, 42, 117–130, 2001.
- Vlaar, N. J., and A. P. van den Berg, Continental evolution and archaeo-sea-levels, in *Glacial Isostasy, Sea-Level and Mantle Rheology*, pp. 637–662, Kluwer Acad., Norwell, Mass., 1991.
- Walter, M. J., Melting of garnet peridotite and the origin of komatiite and depleted lithosphere, *J. Petrol.*, 39, 29–60, 1998.
- Weinberg, R. F., and Y. Podladchikov, Diapiric ascent of magmas through power law crust and mantle, *J. Geophys. Res.*, 99, 9543–9559, 1994.